2022

LENGTH-SCALE-DEPENDENT STRESS RELIEF MECHANISMS IN HIGH PURITY INDIUM

Fereshteh Mallakpour
Michigan Technological University, fmallakp@mtu.edu

LENGTH-SCALE-DEPENDENT STRESS RELIEF MECHANISMS IN HIGH PURITY INDIUM

By

Fereshteh Mallakpour

A DISSERTATION

Submitted in partial fulfillment of the requirements for the degree of

DOCTOR OF PHILOSOPHY

In Materials Science and Engineering

MICHIGAN TECHNOLOGICAL UNIVERSITY

2022

This dissertation has been approved in partial fulfillment of the requirements for the Degree of DOCTOR OF PHILOSOPHY in Materials Science and Engineering.

Department of Materials Science and Engineering

Dissertation Advisor: *Dr. Erik G. Herbert*

Committee Member: *Dr. Stephen A. Hackney.*

Committee Member: *Dr. Stephen L. Kampe.*

Committee Member: *Dr. Gregory M. Odegard.*

Department Chair: *Dr. Walter W. Milligan.*

Table of Contents

List of Figures

List of Tables

Author Contribution Statement

This dissertation contains 4 chapters. The first chapter is the introduction and literature review. The second chapter is published in the Journal of Materials Research and the third chapter is in the process of being submitted for publication. Finally, the last chapter summarized the next steps for this PhD project.

Professor Erik G. Herbert and Professor Stephen A. Hackney have contributed hugely in terms of guidance, advice, discussion regarding data analysis and developing the analytical models for chapter two and chapter three. Also, Professor Erik G. Herbert, Professor Stephen A. Hackney and Dr. P. Sudharshan Phani have contributed to the manuscript development process.

The credit for the FE-SEM images of the residual hardness impressions in chapter two goes to the former ACMAL director, Owen Mill. Also, the credit for the FE-SEM images of etch pit analysis in chapter two and residual hardness impressions in chapter three goes to Dr. Masoud Kasraie.

Acknowledgements

First of all, I would like to thank my advisor, Professor Erik G. Herbert for his support, guidance, and mentorship throughout this Ph.D. project. This work would not be possible without his help and encouragement.

Special thanks to my committee members Professor Stephen A. Hackney, Professor Stephen L. Kampe, and Professor Gregory M. Odegard for serving as my Ph.D. committee members and for their thoughtful comments.

I acknowledge the support that I received from the Materials Science and Engineering Department.

Last but not least, I'm extremely grateful to my beloved husband, Masoud, My Mom and Dad, my brother, Iman, my sister, Adeleh, and my lovely niece Termeh. They always support and encourage me with their unconditional love. I couldn't imagine this journey without them.

Abstract

Lithium-ion batteries are widely used in portable electronics and electric vehicles. However, due to the presence of flammable liquid electrolytes, these devices fail catastrophically when the cell experiences a short circuit. One attractive solution to this problem is a solid-state battery. As the name implies, the flammable liquid electrolyte is replaced by a non-flammable solid-state electrolyte (SSE). The unexpected, yet frequently observed failure mechanism in these devices is the formation and growth of lithium dendrites originating at the interface between the lithium anode and the SSE. As the dendrites grow, device performance degrades. Once the dendrites completely penetrate the SSE, the device short circuits and fails. To better understand the deformation mechanisms controlling the stress concentrations thought to be the precursor to dendrite formation, this dissertation is focused on experimentally identifying the stress relaxation mechanisms operating in small, constrained volumes of high purity metals subjected to high homologous temperatures. To that end, high-purity indium is the model material examined here. Using nanoindentation and electron microscopy, the stress relaxation mechanisms controlling flow have been studied at length scales where the probability of finding dislocations is low. The significant finding is a unique, length-scale dependent competition for stress relief wherein indium, like lithium, is found to be capable of supporting 50 times the expected stress at indentation depths less than 600 nm. In conjunction, nanoindentation creep experiments have been performed within two distinctly different deformation regimes. An analytical model has been developed to rationalize the magnitude of the stress exponent based on the dominant deformation mechanism operating within each regime. Collectively, these results provide significant new insight into the stress relaxation mechanisms operating in small, constrained volumes of crystalline metals subjected to high homologous temperatures.

1 Chapter 1: Introduction

The goal of this research is to develop new knowledge about the deformation mechanisms that control the length scale dependent competition for stress relief in small volumes of bulk indium at a high homologous temperature. Because the mechanical behavior of indium is similar to that of lithium, this knowledge will directly support the engineering of next generation solid-state battery materials designed to solve the dendrite problem, eliminate the formation and growth of lithium dendrites at the interface between a lithium anode and solid electrolyte. Solving the dendrite is a global challenge that has alluded by scientific community for the past 30 years [1-9].

To fulfil the promise of solid-state energy storage, critical gaps need to be filled in understanding the mechanical behavior of lithium at length scales commensurate with the dimensions of morphological defects (e.g., grain boundaries, grain boundary grooves, pores and microcracks) at the interface between a lithium anode and the solid electrolyte separator. The unresolved problem is that inhomogeneous deposition of lithium within these interfacial defects nearly 350 times larger than the nominal yield strength of bulk, polycrystalline lithium [3]. In a manner that depends on the strain rate, the stress intensification within these interfacial defects can cause mode I fracture of the solid electrolyte, thereby, leading to localized mechanical failure that enables the formation and growth of metallic lithium dendrites into the flaw [3-5]. Engineering next generation materials designed to maximize the mechanical stability of the interface will require a complete and comprehensive understanding of the mechanical behavior of lithium as a function of length scale. The difficulty in working with lithium, however, is that it is highly reactive. Even in the controlled atmosphere of a glovebox, pristine lithium surfaces are rendered useless due to contamination within 2-3 days. Rather than coping with the time constraint imposed by lithium's reactivity, well-annealed, high-purity indium was selected as a less reactive mechanical surrogate for lithium. A detailed comparison between indium and lithium is provided in Chapter 2. In summary, the two metals exhibit very similar

mechanical behavior at room temperature, although indium does favor interface rather than volume diffusion due to its lower self-diffusion coefficient.

1.1 Background

1.1.1 Instrumented Indentation

Instrumented indentation or nanoindentation is an experimental technique used to examine the mechanical behavior of small volumes of material. In practice, the measurement system functions as a mechanical properties microprobe. In its most basic form, an indenter tip of some known geometry is driven into the surface of the test specimen. The load is typically controlled (electromagnetic actuation) and the corresponding displacement is measured (3-plate capacitance gauge). After correcting for the instrument's compliances and accounting for thermal drift, the resulting load-displacement data represent the material's mechanical finger print. Among the commonly measured properties are hardness, elastic modulus, and the stress exponent for creep [10]. The most frequently used indenter tip geometries are the Berkovich (3-sided pyramid with a centerline-to-face angle of 65.3°), cube corner (3-sided pyramid with a centerline-to-face angle of 35°), Vickers (4-sided pyramid with a centerline-to-face angle of 68°), cones, spheres and flat punches. Pyramidal and conical indenters are geometrically self-similar. At indentation depths beyond the inevitable rounding at their apex, these indenter tips impose a constant characteristic strain. Indenter tips are generally selected based on the desired test results. Among the self-similar indenter tip geometries, the Berkovich is the workhorse. In comparison to the Vickers, both impose similar strains, but the Berkovich is easier to accurately manufacture to small length scales because the 3 faces inevitably come to a point rather than a line. In comparison to the cube corner, the Berkovich imposes significantly less strain (bigger angle) and minimizes the effects of friction, which is a commonly encountered modeling assumption. Spherical indenter tips find use in applications where their lack of geometric self-similarity enables properties to be measured as a function of strain.

As a pyramidal indenter is driven into the surface of a material, the resulting deformation is elastic-plastic. Theoretical analysis of stress field is very difficult due to the complexities of the non-uniform strain. The most widely used analytical approximation is that of Johnson [11]. Building on the work of Marsh and Hill [12, 13], Johnson proposed the deformation beneath the indenter could be described as a radially expanding cavity comprised of an incompressible hemispherical core subjected to an internal pressure, the so called "expanding cavity" model. This pressure forces the surrounding material to expand radially to accommodate the material displaced by penetration of the indenter. In metals, this hydrostatic stress core grows in a geometrically self-similar fashion dictated by the material's ratio of elastic modulus to yield strength and the material's ability to work harden [11]. Figure 1.1 shows a schematic illustration of the expanding cavity model.

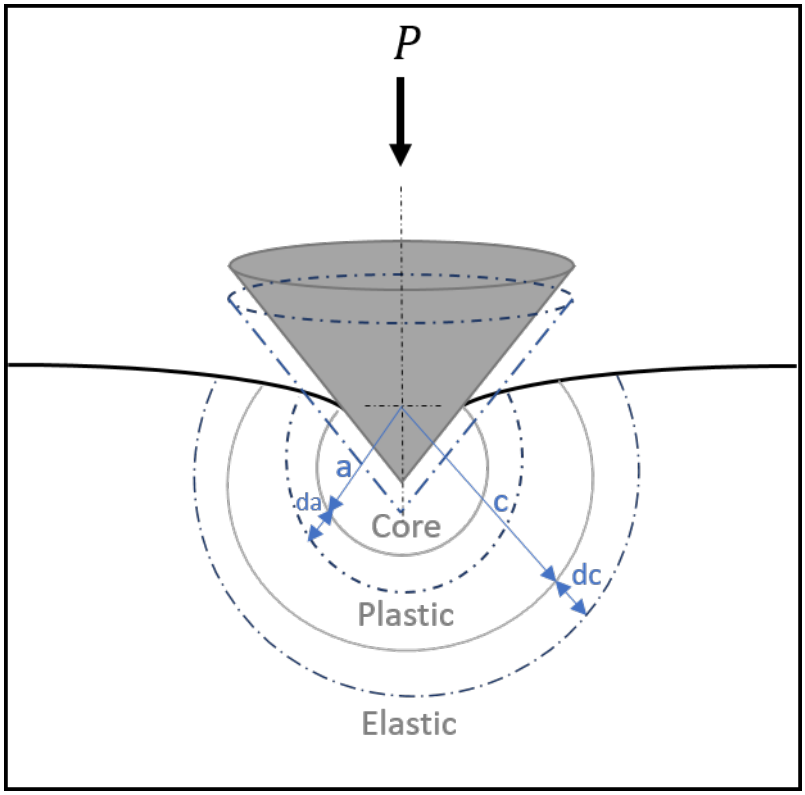

Figure 1.1 The expanding cavity model

Hardness: Calculations and Physical Meaning

The most common definition of hardness, H, from instrumented indentation is

$$H = \frac{P}{A} \tag{1.1}$$

where P is the applied load and A is the projected contact area [10, 14]. Because nanoindentation experiments are typically terminated at indentation depths less than 1 μm, the projected contact area is not generally measured using optical or electron microscopy. Instead, the area is determined based on analytical models used to determine the contact depth, h_c, based on experimentally measured parameters and the geometry of the indenter tip. The ideal mathematical relationship between A and h_c, known as the area function, is shown for several indenter tip geometries in Table 1.1 [10].

Table 1.1. Area function for different tip geometries [10]

Tip Geometry	Projected Contact Area
Berkovich	$A = 24.56h_c^2$
Sphere	$A = 2\pi R h_c$
Cone	$A = \pi \tan^2 \varphi \, h_c^2$
Flat-ended cylinder	$A = \pi r^2$

* R is the indenter tip radius
* φ is the half-included angle of the cone
* r is the radius of the flat punch, $A \neq f(h_c)$

Deviations from the ideal area functions are commonly observed. Particularly at small indentation depths ($h \leq \sim$150 nm) or for small radii spheres ($R \leq \sim$50 μm). Under these conditions, the indenter tip area function is experimentally measured using a reference material with a known elastic modulus.

In addition to hardness, instrumented indentation also routinely yields Young's modulus or the elastic modulus, E, which is calculated directly from a parameter known as the reduced modulus, E_r,

$$E_r = \frac{1}{\beta}\frac{\sqrt{\pi}}{2}\frac{S}{\sqrt{A}} \tag{1.2}$$

where β is a geometric constant based on the indenter tip geometry, S is the elastic contact stiffness (defined as the slope of the unloading curve evaluated at the maximum indentation depth) and A is the projected contact area [10, 14]. In turn, the reduced modulus gives E from

$$E = (1 - \upsilon^2)\left[\frac{1}{E_r} - \frac{1 - \upsilon_i^2}{E_i}\right]^{-1} \tag{1.3}$$

where υ_i and E_i are Poisson's ratio and Young's modulus of the indenter, respectively, υ is the Poisson's ratio of the sample [10, 14].

1.1.2 Indentation Creep

Creep is time-dependent plastic deformation driven by a constant or time varying stress applied at a high homologous temperature. Because creep is a thermally activated process, it can occur at stress levels well below the material's yield strength. The basic form of the constitutive equation describing creep is the power law relation

$$\dot{\varepsilon} = \alpha\sigma^n \tag{1.4}$$

where $\dot{\varepsilon}$ is the steady-state creep rate, α and n are material constants, the creep coefficient and the stress exponent for creep, respectively, σ is the stress, constant. Both α and n are experimentally determined from creep experiments performed on bulk test specimens subjected to uniaxial tension under a constant load. Under steady-state creep conditions, α and n are given by the intercept and slope of a log-log plot of strain rate versus stress. Of

primary interest in this work (Ch. 3), is the relationship between n and the dominant mechanism of action controlling flow. Table 1.2 summarizes these relationships in the context of bulk materials and the mechanisms operating within the stressed volume supporting the indenter tip [15].

Table 1.2.Characteristic creep mechanisms.

n	**Mechanisms**
Intragranular dislocation mechanisms	
1	Harper-Dorn creep
3	Dislocation glide
≥ 4.5	Dislocation climb
Diffusional creep & vacancy flow	
1	Nabarro-Herring creep

Nanoindentation studies of creep typically adopt the same constitutive relationship, Eq. (1.4). However, unique differences in the test geometry do not permit a direct correlation between the creep coefficient, α, measured in uniaxial tension and nanoindentation [16]. The stress exponent, n on the other hand, has been found to correlate well, but only in the limit of creep governed by dislocation glide and climb. Prior to the work presented in Ch. 3, only one indentation study has attempted to correlate n when diffusion is the dominant flow mechanism [17]. Under those conditions, the authors argue $n = 1$ regardless of the test geometry (bulk versus nanoindentation). Through the analysis and results presented in Chs. 2 and 3, this dissertation presents a unique diffusional flow model that contradicts this poorly founded convention. It predicts $n \neq 1$ for nanoindentation and, moreover, that n depends on the indenter tip geometry.

1.1.3 Beyond Li-ion Batteries

Because of their high specific energy density and low weight, lithium batteries are used for portable electronic devices and electric vehicles [18-20]. However, the conventional liquid electrolytes used to separate the battery's electrodes are flammable, leading to catastrophic

failures when the devices short circuit [21]. A potential solution to this problem is the solid-state battery [9, 21]. As the name implies, all the components of the battery, including the electrolyte are solids. Non-flammable solid electrolytes significantly improve safety and directly enable the use of a pure metallic lithium anode, thus, potentially yielding the safest, lightest and smallest batteries possible [21].

Traditional battery research generally focuses on the optimization of energy, power, capacity, interfacial resistance, ionic conductivity, cycle life etc. While each of these metrics is vital to solid-state battery (SSBs) performance, it has become apparent that the mechanical stability of each component and their corresponding interfaces is equally important. Practical experience with prototype solid state lithium metal batteries has shown that lithium has a remarkable propensity to penetrate and fracture even the strongest electrolyte materials. This unexpected outcome highlights a significant barrier to realizing the full potential of this transformative technology. Engineering materials to solve this problem will require filling critical knowledge gaps. Among them is understanding how and why some stress concentrations at the interface between a lithium anode and a solid electrolyte can exceed the bulk yield strength of lithium by more than two orders of magnitude. The extent to which this knowledge gaps can be filled will provide direct insight into the stresses that must be relieved by materials engineered to enable next generation devices.

1.1.3.1 Lithium dendrite formation and growth

Over the past 10 years, different approaches have been taken to prevent the formation and growth of lithium dendrites originating at the interface between a lithium anode and a solid electrolyte separator [22]. The most widely adopted approach today is the use of a ceramic separator comprised of lithium, lanthanum, zirconia, and oxygen with minor additions of aluminum or tantalum, known as LLZO. This separator was chosen because of its relatively high ionic conductivity and its perceived ability to function as the proverbial brick wall, mechanically suppressing the formation and growth of lithium dendrites through its high elastic modulus (~150 GPa). However, the experimental work of Cheng et al. [23]

demonstrated that metallic lithium is fully capable of penetrating completely through LLZO by propagating along its grain boundaries. When the grain boundaries are removed (single crystal LLZO), metallic lithium simply finds another morphological defect at the interface to exploit. As the localized stress increases, the defect propagates through the LLZO until the device fails by short circuiting. These observations raise a critical question. How does lithium force a ceramic separator to fail by fracture?

As reported by Xu et *al*. [8], the yield strength of lithium micropillars loaded in uniaxial compression is inversely proportional to the diameter of pillar. The yield strength, defined as the stress at which the first significant strain burst occurs, increases from 15 to 105 MPa as the pillar diameter decreases from 9.45 to 1.39 μm. Xu et *al*. conclude that the room temperature size effect can be rationalized by one of two mechanisms: Dislocation multiplication-driven plasticity or, dislocation nucleation-governed plasticity (frequently observed in single crystalline metals at small length scales) [8]. While Xu was the first to experimentally observe the length scale dependent strength of lithium, he did not offer a detailed mechanistic rationalization beyond dislocation nucleation.

1.1.3.2 Understanding the competition for stress relief through nanoindentation

During charging, lithium ions travel through the separator and plate to the anode. Ideally, the plating occurs one atomic layer at a time and in a manner that is nominally stress free. In reality, any morphological deviations from a planar interface between the anode and separator create a gradient in the chemical potential that drives the incoming lithium ions to preferentially plate out into the defects [24]. This preferential diffusion of lithium results in a competition for stress relief. In the absence of mobile dislocations or operable dislocation multiplication sources within the stressed volume, other stress relief mechanisms are naturally activated. Among these are stress directed self-diffusion of lithium and fracture of the solid electrolyte separator. When lithium's diffusion mechanisms become overwhelmed due to high strain rates and or long diffusion distances, then diffusive flow becomes ineffective, thus, favoring fracture of the separator.

To better understand the stress lithium can support under these conditions, nanoindentation experiments were performed in high-purity lithium films [2-4]. Figure 1.2 shows the measured hardness as a continuous function of depth and strain rate. The colored lines represent rationalizations of the depth and strain rate dependent hardness based on volume diffusion to the free surface (Nabarro-Herring) and non-conservative dislocation motion (Harper-Dorn). At slower strain rates, the mean pressure (hardness) increases with depth due to the increase in the diffusion length. As the strain rate increases, volume diffusion becomes less efficient due to time constraints and, therefore, the pressure increases with strain rate. At the highest strain rate, volume diffusion becomes effectively inoperable and forces the stress relief to revert to non-conservative dislocation motion, which is very inefficient at small length scales, but becomes increasingly efficient as the stressed volume increases, as shown by the observed decrease in pressure with depth. The discernable kink in each data set is representative of the transition from diffusion to shear driven dislocation glide. In a manner that depends on the length scale and strain rate, these data show the pressure with lithium filled interface defects is capable of reaching on the order of 200 MPa [3].

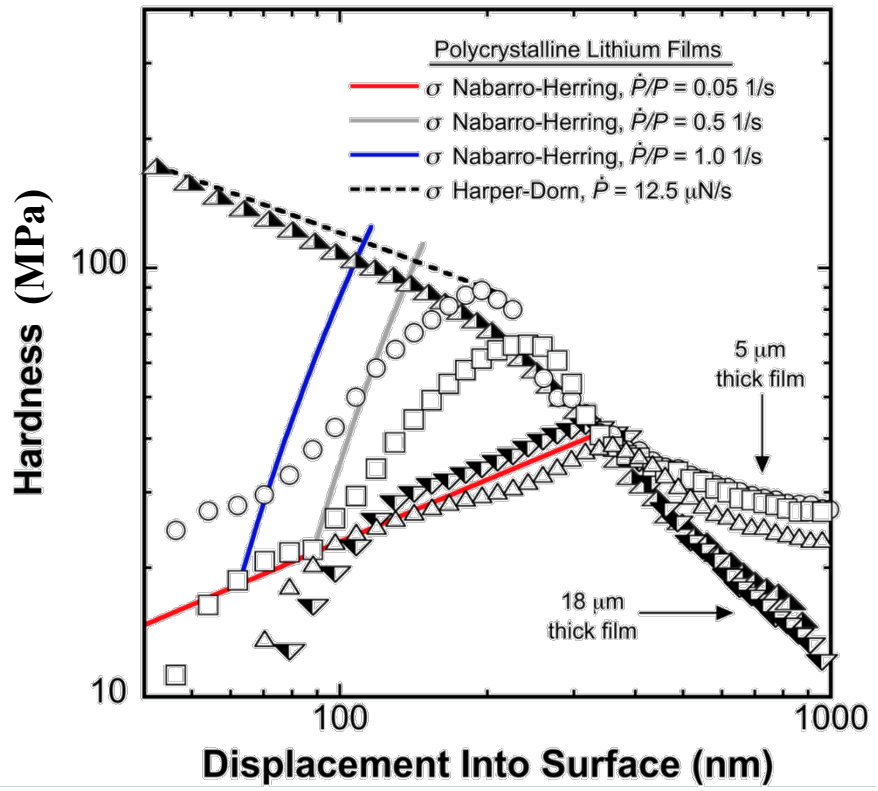

Figure 1.2. Hardness vs. depth for Li thin films (different strain rates) [3]

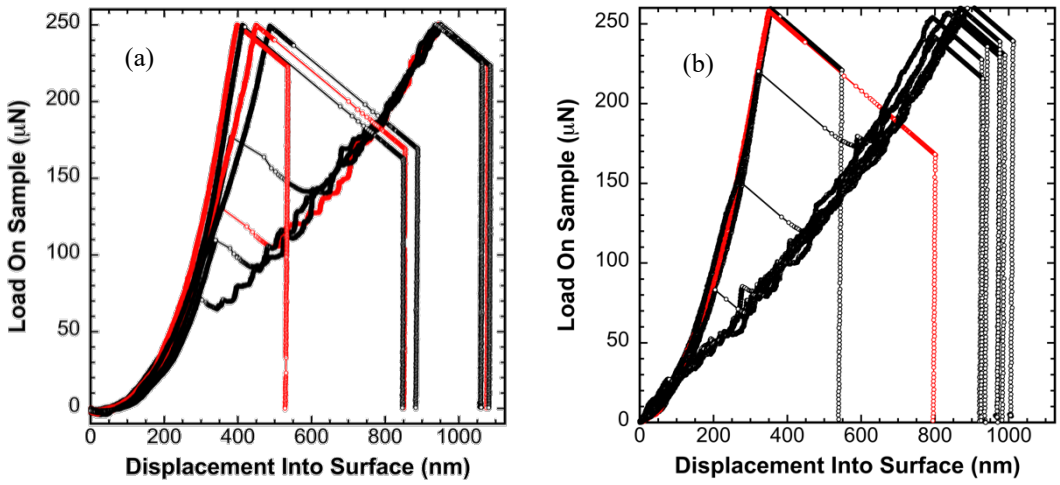

Figure 1.3. Representative load-displacement curves in high-purity lithium at a homologous temperature of 0.67. (a) Targeted strain rate of 0.05 1/s. (b) Prescribed loading rate of 12.5 μN/s, which translates into an indentation strain rate that is 7× the rate observed in (a) [3]

The corresponding load-displacement data further support the hardness-depth rationalizations described above. Figure 1.3 (a) and (b) show representative load-displacement curves obtained at the lowest and highest indentation strain rates, respectively. As the data show, both strain rates exhibit an abrupt transition from relatively smooth, monotonically increasing load-displacement behavior to discernably serrated flow. Given the high homologous temperature, it has been proposed that before the transition (signaled by the strain burst and subsequent drop in pressure), the dominant flow mechanism is stress directed diffusion. After the transition, the flow mechanism reverts to dislocation mediated glide. The serrated flow is taken to be characteristic of the stick-slip behavior observed when dislocations pile-up against barriers such as other dislocations, pinning points, and/or grain boundaries. The stochastic nature of the strain burst itself suggests the operation of dislocation multiplication source that requires achieving a threshold in stress and sufficient room to physically operate. Collectively, these experimental observations provide unique insight into the length scale and strain rate

dependent competition for stress relief in constrained, small volumes of crystalline metals subjected to high homologous temperatures [3, 25, 26].

Direct microstructural evidence of the dislocation density before and after the strain burst would provide the most conclusive proof of the proposed rationalizations. The challenges associated with creating suitable specimens for the transmission electron microscope (TEM) and engineering environmentally controlled systems to enable contamination-free transfer between the glovebox and TEM are deemed insurmountable. As an alternative, Chs. 2 and 3 of this dissertation present complimentary experimental evidence obtained in well-annealed, high-purity indium. As explained in Ch. 2, indium was selected for this investigation because of its stability in ambient conditions and its ability to serve as a mechanical surrogate for lithium. In Ch. 2, analyses of the residual hardness impressions from before the strain burst become the foundation for a new model describing how conservation of volume is achieved through pile-up resulting from interface diffusion, which is taken to be the mechanism of action controlling stress relief before the strain burst. In Ch. 3, constant load and hold creep experiments are used to determine the stress exponent for creep both before and after the strain burst. A new model is presented to rationalize the measured stress exponent before the strain burst based on interface diffusion. After the burst, the measured stress exponent is rationalized in terms dislocation mediated glide and climb with consideration of the indentation size effect. Chapter 4 concludes this dissertation with a summary discussion of the next steps. It identifies critical knowledge gaps, presents general hypotheses, and outlines the basic experiments required to test the proposed hypotheses.

1.2 References

1. Cheng, L., et al., *Effect of surface microstructure on electrochemical performance of garnet solid electrolytes.* ACS applied materials & interfaces, 2015. **7**(3): p. 2073-2081.
2. Herbert, E.G., et al., *Nanoindentation of high-purity vapor deposited lithium films: The elastic modulus.* Journal of Materials Research, 2018. **33**(10): p. 1335-1346.
3. Herbert, E.G., et al., *Nanoindentation of high-purity vapor deposited lithium films: A mechanistic rationalization of diffusion-mediated flow.* Journal of Materials Research, 2018. **33**(10): p. 1347-1360.
4. Herbert, E.G., et al., *Nanoindentation of high-purity vapor deposited lithium films: A mechanistic rationalization of the transition from diffusion to dislocation-mediated flow.* Journal of Materials Research, 2018. **33**(10): p. 1361-1368.
5. Porz, L., et al., *Mechanism of lithium metal penetration through inorganic solid electrolytes.* Advanced Energy Materials, 2017. **7**(20): p. 1701003.
6. Sharafi, A., et al., *Controlling and correlating the effect of grain size with the mechanical and electrochemical properties of Li 7 La 3 Zr 2 O 12 solid-state electrolyte.* Journal of Materials Chemistry A, 2017. **5**(40): p. 21491-21504.
7. Sharafi, A., et al., *Characterizing the Li–Li7La3Zr2O12 interface stability and kinetics as a function of temperature and current density.* Journal of Power Sources, 2016. **302**: p. 135-139.
8. Xu, C., et al., *Enhanced strength and temperature dependence of mechanical properties of Li at small scales and its implications for Li metal anodes.* Proceedings of the National Academy of Sciences, 2017. **114**(1): p. 57-61.
9. Yu, S., et al., *Elastic properties of the solid electrolyte Li7La3Zr2O12 (LLZO).* Chemistry of Materials, 2016. **28**(1): p. 197-206.
10. Hay, J., *Introduction to instrumented indentation testing.* Experimental techniques, 2009. **33**(6): p. 66-72.
11. Johnson, K., *The correlation of indentation experiments.* Journal of the Mechanics and Physics of Solids, 1970. **18**(2): p. 115-126.
12. Hill, R., *The mathematical theory of plasticity, Clarendon.* Oxford, 1950. **613**: p. 614.
13. Marsh, D., *Plastic flow in glass.* Proceedings of the Royal Society of London. Series A. Mathematical and Physical Sciences, 1964. **279**(1378): p. 420-435.
14. Oliver, W.C. and G.M. Pharr, *An improved technique for determining hardness and elastic modulus using load and displacement sensing indentation experiments.* Journal of materials research, 1992. **7**(6): p. 1564-1583.
15. Choi, I.-C., et al., *Indentation creep revisited.* Journal of Materials Research, 2012. **27**(1): p. 3-11.
16. Bower, A., et al., *Indentation of a power law creeping solid.* Proceedings of the Royal Society of London. Series A: Mathematical and Physical Sciences, 1993. **441**(1911): p. 97-124.

17. Feng, G. and A. Ngan, *Creep and strain burst in indium and aluminium during nanoindentation.* Scripta materialia, 2001. **45**(8): p. 971-976.
18. Armand, M. and J.-M. Tarascon, *Building better batteries.* nature, 2008. **451**(7179): p. 652-657.
19. Bae, J., et al., *A 3D nanostructured hydrogel-framework-derived high-performance composite polymer lithium-ion electrolyte.* Angewandte Chemie International Edition, 2018. **57**(8): p. 2096-2100.
20. Gerssen-Gondelach, S.J. and A.P. Faaij, *Performance of batteries for electric vehicles on short and longer term.* Journal of power sources, 2012. **212**: p. 111-129.
21. Swamy, T., et al., *Lithium metal penetration induced by electrodeposition through solid electrolytes: example in single-crystal Li6La3ZrTaO12 garnet.* Journal of The Electrochemical Society, 2018. **165**(16): p. A3648.
22. Xu, W., et al., *Lithium metal anodes for rechargeable batteries.* Energy & Environmental Science, 2014. **7**(2): p. 513-537.
23. Cheng, E.J., A. Sharafi, and J. Sakamoto, *Intergranular Li metal propagation through polycrystalline Li6. 25Al0. 25La3Zr2O12 ceramic electrolyte.* Electrochimica Acta, 2017. **223**: p. 85-91.
24. Dudney, N.J., *Approaches toward lithium metal stabilization.* MRS Bulletin, 2018. **43**(10): p. 752-758.
25. Nix, W.D. and H. Gao, *Indentation size effects in crystalline materials: a law for strain gradient plasticity.* Journal of the Mechanics and Physics of Solids, 1998. **46**(3): p. 411-425.
26. Pharr, G.M., E.G. Herbert, and Y. Gao, *The indentation size effect: a critical examination of experimental observations and mechanistic interpretations.* Annual Review of Materials Research, 2010. **40**: p. 271-292.

A Appendix 1.A. Reprint Copyright Permission

Figure 1.2 and Figures 1.3 (a) and (b) used in Chapter 1 were originally published in "Nanoindentation of high-purity vapor deposited lithium films: A mechanistic rationalization of diffusion-mediated flow." *Journal of Materials Research 33.10 (2018): 1347-1360*. A copy of the copyright permission is shown below.

SPRINGER NATURE LICENSE
TERMS AND CONDITIONS

Oct 11, 2022

This Agreement between Michigan Tech University -- Fereshteh Mallakpour ("You") and Springer Nature ("Springer Nature") consists of your license details and the terms and conditions provided by Springer Nature and Copyright Clearance Center.

License Number	5405991230750
License date	Oct 11, 2022
Licensed Content Publisher	Springer Nature
Licensed Content Publication	Journal of Materials Research
Licensed Content Title	Nanoindentation of high-purity vapor deposited lithium films: A mechanistic rationalization of diffusion-mediated flow
Licensed Content Author	Erik G. Herbert et al
Licensed Content Date	May 1, 2018
Type of Use	Thesis/Dissertation
Requestor type	academic/university or research institute
Format	print and electronic
Portion	figures/tables/illustrations
Number of figures/tables/illustrations	3

Will you be translating?	no
Circulation/distribution	50000 or greater
Author of this Springer Nature content	no
Title	LENGTH SCALE-DEPENDENT STRESS RELIEF MECHANISMS IN HIGH PURITY INDIUM
Institution name	Michigan Technological University
Expected presentation date	Nov 2022
Portions	Figure 3, Figure 4, and Figure 8
Requestor Location	Michigan Tech University 1400 Townsend Dr. HOUGHTON, MI 49931 United States Attn: Michigan Tech University
Total	0.00 USD

Terms and Conditions

Springer Nature Customer Service Centre GmbH
Terms and Conditions

This agreement sets out the terms and conditions of the licence (the **Licence**) between you and **Springer Nature Customer Service Centre GmbH** (the **Licensor**). By clicking 'accept' and completing the transaction for the material (**Licensed Material**), you also confirm your acceptance of these terms and conditions.

1. Grant of License

1. 1. The Licensor grants you a personal, non-exclusive, non-transferable, world-wide licence to reproduce the Licensed Material for the purpose specified in your order only. Licences are granted for the specific use requested in the order and for no other

use, subject to the conditions below.

1. 2. The Licensor warrants that it has, to the best of its knowledge, the rights to license reuse of the Licensed Material. However, you should ensure that the material you are requesting is original to the Licensor and does not carry the copyright of another entity (as credited in the published version).

1. 3. If the credit line on any part of the material you have requested indicates that it was reprinted or adapted with permission from another source, then you should also seek permission from that source to reuse the material.

2. Scope of Licence

2. 1. You may only use the Licensed Content in the manner and to the extent permitted by these Ts&Cs and any applicable laws.

2. 2. A separate licence may be required for any additional use of the Licensed Material, e.g. where a licence has been purchased for print only use, separate permission must be obtained for electronic re-use. Similarly, a licence is only valid in the language selected and does not apply for editions in other languages unless additional translation rights have been granted separately in the licence. Any content owned by third parties are expressly excluded from the licence.

2. 3. Similarly, rights for additional components such as custom editions and derivatives require additional permission and may be subject to an additional fee. Please apply to Journalpermissions@springernature.com/bookpermissions@springernature.com for these rights.

2. 4. Where permission has been granted **free of charge** for material in print, permission may also be granted for any electronic version of that work, provided that the material is incidental to your work as a whole and that the electronic version is essentially equivalent to, or substitutes for, the print version.

2. 5. An alternative scope of licence may apply to signatories of the STM Permissions Guidelines, as amended from time to time.

3. Duration of Licence

3. 1. A licence for is valid from the date of purchase ('Licence Date') at the end of the relevant period in the below table:

Scope of Licence	Duration of Licence
Post on a website	12 months
Presentations	12 months
Books and journals	Lifetime of the edition in the language purchased

4. Acknowledgement

4. 1. The Licensor's permission must be acknowledged next to the Licenced Material in print. In electronic form, this acknowledgement must be visible at the same time as the figures/tables/illustrations or abstract, and must be hyperlinked to the journal/book's homepage. Our required acknowledgement format is in the Appendix below.

5. Restrictions on use

5. 1. Use of the Licensed Material may be permitted for incidental promotional use and minor editing privileges e.g. minor adaptations of single figures, changes of format, colour and/or style where the adaptation is credited as set out in Appendix 1 below. Any other changes including but not limited to, cropping, adapting, omitting material that affect the meaning, intention or moral rights of the author are strictly prohibited.

5. 2. You must not use any Licensed Material as part of any design or trademark.

5. 3. Licensed Material may be used in Open Access Publications (OAP) before publication by Springer Nature, but any Licensed Material must be removed from OAP sites prior to final publication.

6. Ownership of Rights

6. 1. Licensed Material remains the property of either Licensor or the relevant third party and any rights not explicitly granted herein are expressly reserved.

7. Warranty

IN NO EVENT SHALL LICENSOR BE LIABLE TO YOU OR ANY OTHER PARTY OR ANY OTHER PERSON OR FOR ANY SPECIAL, CONSEQUENTIAL, INCIDENTAL OR INDIRECT DAMAGES, HOWEVER CAUSED, ARISING OUT OF OR IN CONNECTION WITH THE DOWNLOADING, VIEWING OR USE OF THE MATERIALS REGARDLESS OF THE FORM OF ACTION, WHETHER FOR BREACH OF CONTRACT, BREACH OF WARRANTY, TORT, NEGLIGENCE, INFRINGEMENT OR OTHERWISE (INCLUDING, WITHOUT LIMITATION, DAMAGES BASED ON LOSS OF PROFITS, DATA, FILES, USE, BUSINESS OPPORTUNITY OR CLAIMS OF THIRD PARTIES), AND
WHETHER OR NOT THE PARTY HAS BEEN ADVISED OF THE POSSIBILITY OF SUCH DAMAGES. THIS LIMITATION SHALL APPLY NOTWITHSTANDING ANY FAILURE OF ESSENTIAL PURPOSE OF ANY LIMITED REMEDY PROVIDED HEREIN.

8. Limitations

8. 1. ***BOOKS ONLY:*** Where **'reuse in a dissertation/thesis'** has been selected the following terms apply: Print rights of the final author's accepted manuscript (for clarity, NOT the published version) for up to 100 copies, electronic rights for use only on a personal website or institutional repository as defined by the Sherpa guideline

(www.sherpa.ac.uk/romeo/).

8. 2. For content reuse requests that qualify for permission under the STM Permissions Guidelines, which may be updated from time to time, the STM Permissions Guidelines supersede the terms and conditions contained in this licence.

9. Termination and Cancellation

9. 1. Licences will expire after the period shown in Clause 3 (above).

9. 2. Licensee reserves the right to terminate the Licence in the event that payment is not received in full or if there has been a breach of this agreement by you.

Appendix 1 — Acknowledgements:

For Journal Content:
Reprinted by permission from [**the Licensor**]: [**Journal Publisher** (e.g. Nature/Springer/Palgrave)] [**JOURNAL NAME**] [**REFERENCE CITATION** (Article name, Author(s) Name), [**COPYRIGHT**] (year of publication)

For **Advance Online Publication papers:**
Reprinted by permission from [**the Licensor**]: [**Journal Publisher** (e.g. Nature/Springer/Palgrave)] [**JOURNAL NAME**] [**REFERENCE CITATION** (Article name, Author(s) Name), [**COPYRIGHT**] (year of publication), advance online publication, day month year (doi: 10.1038/sj.[JOURNAL ACRONYM].)

For Adaptations/Translations:
Adapted/Translated by permission from [**the Licensor**]: [**Journal Publisher** (e.g. Nature/Springer/Palgrave)] [**JOURNAL NAME**] [**REFERENCE CITATION** (Article name, Author(s) Name), [**COPYRIGHT**] (year of publication)

Note: For any republication from the British Journal of Cancer, the following credit line style applies:

Reprinted/adapted/translated by permission from [**the Licensor**]: on behalf of Cancer Research UK: : [**Journal Publisher** (e.g. Nature/Springer/Palgrave)] [**JOURNAL NAME**] [**REFERENCE CITATION** (Article name, Author(s) Name), [**COPYRIGHT**] (year of publication)

For **Advance Online Publication** papers:
Reprinted by permission from The [**the Licensor**]: on behalf of Cancer Research UK: [**Journal Publisher** (e.g. Nature/Springer/Palgrave)] [**JOURNAL NAME**] [**REFERENCE CITATION** (Article name, Author(s) Name), [**COPYRIGHT**] (year of publication), advance online publication, day month year (doi: 10.1038/sj.[JOURNAL ACRONYM])

For Book content:
Reprinted/adapted by permission from [**the Licensor**]: [**Book Publisher** (e.g. Palgrave Macmillan, Springer etc) [**Book Title**] by [**Book author**(s)] [**COPYRIGHT**] (year of publication)

2 Chapter 2: Length Scale Dependent Stress Relief Mechanisms in Indium at High Homologous Temperatures

Published in JMR- DOI: 10.1557/s43578-021-00186-6

2.1 Abstract

Nanoindentation and electron microscopy have been used to examine the length-scale dependent stress relaxation mechanisms in well-annealed, high purity indium at a homologous temperature of 0.69. The experimental methods, analysis and observations serve as a stepping stone in identifying the stress relaxation mechanisms enabling the formation and growth of metallic dendrites originating at the buried interface between a metallic anode and a solid electrolyte separator. Indium's load-displacement data are found to be very similar to that of high-purity lithium. Residual hardness impressions show two distinct surface morphologies. Based on these morphologies, the measured hardness and the estimated pile-up volume, it is proposed that residual impressions exhibiting significant pile-up are the result of deformation dominated by interface diffusion. Alternatively, impressions with no significant pile-up are taken to be the result of shear driven dislocation glide. An analytical model is presented to rationalize the pile-up profile using interface diffusion.

2.2 Introduction

The use of nanoindentation to examine mechanical behavior at high homologous temperatures offers unique insights into creep processes at small length scales. Small length scale creep is particularly important at non-planar interfaces between materials of different homologous temperatures, where a discontinuity in the bulk plastic relaxation mechanism can result in complex length-scale and strain rate dependent mechanisms controlling the relaxation of stress gradients [1]. This has recently been demonstrated for the process of lithium metal nanoindentation at room temperature and related to the mechanical stability of the interface between a solid-state electrolyte (SSE) and the lithium metal negative electrode (anode) in solid-state batteries [1-3]. As previously reported, the self-limiting behavior of lithium at small length scales, where the probability of finding mobile dislocations or operable dislocation multiplication sources is low, is governed by a unique competition for stress relief between stress directed diffusional flow and shear driven dislocation glide. Within this poorly understood and minimally documented regime, the flow stress (hardness) of lithium is found to be strongly dependent on the strain rate and length scale (indentation depth) [2, 3].

In this paper, we carry out a nanoindentation study of well-annealed, high purity indium as a way to verify the previously reported lithium results using a more chemically stable surrogate, as indium has a standard electrode potential between -0.34 and -0.49 V versus the standard hydrogen electrode (SHE) while lithium has a standard electrode potential of -3.04 V versus SHE [4]. Moreover, the chemical stability of indium (relative to lithium) enables the utilization of additional imaging techniques outside the controlled atmosphere of an inert glove box. Table 2.1 directly compares the relevant physical, mechanical and thermal properties of both indium and lithium [5]. While indium is clearly not a relevant anode material, the goal of this investigation is to document the experimental methods, observations and rationalizations associated with the operation and identification of specific stress relaxation mechanisms in a high purity, crystalline metal at a high homologous temperature and "small" length scales (indentation depths $\leq \sim 1$ μm). In

addition to its chemical stability, we note indium is particularly well suited for this purpose because it enables testing at high homologous temperatures without the complications of conducting high temperature nanoindentation testing. In this way, the results reported here serve as a comparative stepping stone, enabling a more complete and comprehensive understanding of small length scale creep, particularly as it relates to candidate anode materials, i.e., lithium and sodium, at length scales commensurate with the formation and growth of metallic filaments or dendrites.

In comparison to well-annealed elemental metals at low homologous temperatures, the load-displacement "pop-in" events observed in indium are entirely unique [6, 7]. The pop-ins observed here and reported elsewhere do not represent the transition from elastic to elastic-plastic deformation, but rather an abrupt transition in the mechanism by which flow occurs in well-annealed, high purity indium [6]. Collectively, the data presented here are generally consistent with the strain rate and length scale dependent competition for stress relief previously reported in high purity lithium. Prior to the pop-in event observed during nanoindentation, we submit the primary distinction between indium and lithium is the mechanism that controls flow, which we propose is interface rather than volume diffusion, respectively [8, 9]. While the results presented here provide unique insight into the stress directed diffusional flow of indium, there are still many unanswered questions. Chief among them is a meaningful examination of strain rate effects in the limit of stress directed diffusional flow, which awaits the evolution of constant strain rate testing capability under these unique deformation conditions.

Table 2.1. Constants & properties of bulk indium and lithium and the interface diffusion model constants for indium.

Constant/Property & Model Constants	Indium	Lithium
crystal structure	BCT	BCC
ρ (g/cm^3), density	7.30	0.534
E (GPa), elastic modulus[1]	12.7	9.5
G (GPa), shear modulus	3.8	4.25
ν (-), Poisson's ratio	0.45	0.362
σ_y (MPa), yield stress	0.93	0.5
T_m (ºC), melting temperature	156.6	180.5
D_o (m^2/s), pre-exponential term	3.2×10^{-4}	2.3×10^{-5}
Q_d (J), activation energy for self-diffusion	78300	55300
T (ºC), test temperature	24.4	
T_H (-), homologous temperature at 24.4 ºC	0.69	0.66
D (m^2/s), self-diffusion coefficient	5.7×10^{-18}	4.5×10^{-15}
D_s (m^2/s), surface diffusivity	5×10^{-11}	NA
δ (m), surface layer thickness	1×10^{-9}	NA
Ω (m^3/atom), atomic volume	2.6×10^{-29}	NA
γ (J/m^2), surface energy	1	NA
V (m/s), triple point velocity	1×10^{-8}	NA
H (J/m^3), hardness	5.4×10^{7}	NA
ω (1/m), elastic relaxation length	1.2×10^{6}	NA
k_B (J/(atom·K))	1.38×10^{-23}	NA

[1] The elastic modulus of lithium is highly anisotropic

2.3 Experimental Methods

2.3.1 Preparation of well-annealed, high-purity indium

The nanoindentation test specimen (~20×15×3 mm) was cast from 99.999% pure indium shot (Indium Corporation, Clinton, New York). Approximately 15, 3 mm pellets were melted in a quartz crucible on a hot plate at ~200 ºC. To eliminate adhesion between the cast indium and substrate, the molten indium was poured directly onto a room temperature

aluminum block (diameter = 25.4 cm, thickness = 7.6 cm) covered with Kapton tape ~1 mm thick. Within minutes of casting, the indium specimen was enclosed in an evacuated quartz tube and annealed for 6 hours at 110 ºC (a homologous temperature of 0.89). At short wavelengths, the annealed, as-cast surface finish enabled reproducible load-displacement curves at indentation depths as small as 10 nm. Using a thin layer of two-part epoxy resin, the annealed, as-cast indium specimen was mounted onto glass slides (2×2 cm) previously crystal bonded (thermal set wax) to the instrument's 1.25-inch aluminum specimen mounts.

In the interest of informing future experimentalists, we note that longer wavelength undulations in the as-cast surface made it practically impossible to successfully run multiple arrays within a single batch of experiments. A potential solution to this problem was recently presented by Fincher et al., who utilized lubricated glass slides and a benchtop vice to create parallel top and bottom surfaces of a sodium test specimen [10]. Although implementing this approach with indium will require extensive annealing, this path is particularly attractive in that it potentially provides a means to achieving a large test surface that is both smooth and flat.

2.3.2 Nanoindentation

Room temperature nanoindentation experiments were performed using a Berkovich diamond indenter tip mounted in the InForce50 nanomechanical actuator (Nanomechanics, Inc.-KLA Tencor, Oak Ridge, Tennessee). Twenty-five measurements were targeted in a 5×5 array with 30 μm spacing in the x and y directions. The maximum load was prescribed at 700 μN and the loading was controlled such that the ratio of $\dot{P}/P$ was targeted at the user defined value of 0.1 s^{-1}. The loading was performed in 3 cycles. The first two unloaded partially (50%) from 175 and 350 μN while the final cycle unloaded completely from 700 μN. Given the high homologous temperature and the specimen's propensity to creep, no attempt was made to measure the thermal drift rate or correct the measured displacement for thermal drift. To help mitigate the effect of drift, the environment's thermal stability was maximized by utilizing an 8-hour start delay and running the experiments overnight.

Furthermore, the selected load-time history allowed each individual test to be executed in less than 60 s.

2.3.3 Scanning Electron Microscopy

Images of the residual hardness impressions and etch pits were obtained using a field emission high resolution scanning electron microscope, the Hitachi S-4700 FE-SEM (Schaumburg, IL, USA). This microscope was also used to perform the energy dispersive X-ray spectroscopy and deposit the carbon line scan. With the carbon line oriented parallel to the y-axis of the SEM stage, the vertical height of the pile-up profile, z, was calculated as a function of position along the y-axis using the relation $z = \Delta x / \sin\theta$, where Δx is the directly measured change in position along the x-axis and θ is the y-axis tilt, which was 45°. For the pile-up dimensions examined here, this technique provides a simple, quantitative means of determining the pile-up height without requiring built-in tilt corrections from the microscope.

2.3.4 Etch Pit Analysis

Following nanoindentation, the indium specimen was iteratively etched in 3, 4-minute intervals using a 10% nitric acid solution. The etch pit density (EPD) was measured from an area approximately 0.03 mm^2 located directly below the 5×5 array of residual hardness impressions. Following each iteration, the EPD was measured using an Olympus BX51M (Center Valley, PA, USA) optical microscope and the image analysis software, ImageJ. The Hitachi S-4700 FE-SEM was used to examine the morphology and faceting of several etch pits. Following iterations 2 and 3, the EPD decreased, as several pits disappeared, others combined and several grew. Thus, the most accurate estimate of the EPD, 7.09×10^4 cm^{-2}, was determined from the first 4-minute interval. The subsequent decrease in the EPD with time is taken to be the result of over etching. As shown in Figure 2.3 (a), it is interesting to note that there are no discernable pits in close proximity to the residual hardness impressions – neither the ones that experienced a strain burst, nor the ones that

did not. One potential explanation is that dislocations created by the strain burst may have annealed out. Due to the COVID-19 pandemic, the EPD was not measured until 6 months after the indentation experiments were performed. Given the high T_H of 0.69, it is possible that over 6 months, the recovery process and a diffusion length of ~9.5 μm may have eliminated any dislocations created by the strain burst. Following the previously presented argument made by Rester et al., it is also possible that following the transition or pop-in, an intrinsic ISE does play a role in that GNDs caused by the indentation geometry have coalesced into cell walls or subgrains [11]. Presumably the subgrains would develop directly beneath the indenter tip, as the GNDs would be limited to operating within the local gradient in strain. In this way, the GNDs would not be visible at the free surface and, thus, not discernable by etch pit analysis techniques.

2.4 Experimental Observations and Discussion

2.4.1 Load-Displacement Curves

Figure 2.1 shows 8 cyclic load-displacement, $P-h$, curves from a total of 25 measurements performed at a homologous temperature, T_H, of 0.69. Among these representative curves, four exhibit a significant strain burst or "pop" and four do not. Considering the four curves that do pop, we note the stochastic nature of the event, as two curves pop between the first and second load-unload cycle, while the other two pop between the second cycle and final unload. Although not explicitly shown in Figure 2.1, none of the 25 $P-h$ curves exhibit a strain burst before completing the first load-unload cycle. Since the first cycle clearly exhibits elastic-plastic deformation (dominated by plasticity), we conclude the observed strain bursts are not representative of the onset of plastic deformation, but rather an abrupt, albeit stochastic transition in the stress relaxation mechanism by which indium accommodates plasticity under the imposed testing conditions. As a point of reference, the dashed black line originating at the origin illustrates the theoretical elastic $P-h$ curve for a sharp equivalent cone (half-included angle $=$

70.32°) [1, 2]. As per Table 2.1, the theoretical curve assumes $E = 12.7$ GPa and $\nu = 0.45$. As the plot shows, the elastic limit clearly indicates the measured $P - h$ curves are representative of elastic-plastic deformation.

For comparative purposes, Figure 2.2 shows the unique similarities between representative $P - h$ curves for both indium and lithium (both near room temperature and subjected to similar strain rates). Specifically, we note the monotonically increasing load followed by the abrupt strain burst, serrated flow, extensive creep (see reference [2]) and the nearly vertical unload. These similarities suggest that near room temperature, high purity indium and lithium accommodate plastic deformation by utilizing similar stress relaxation mechanisms.

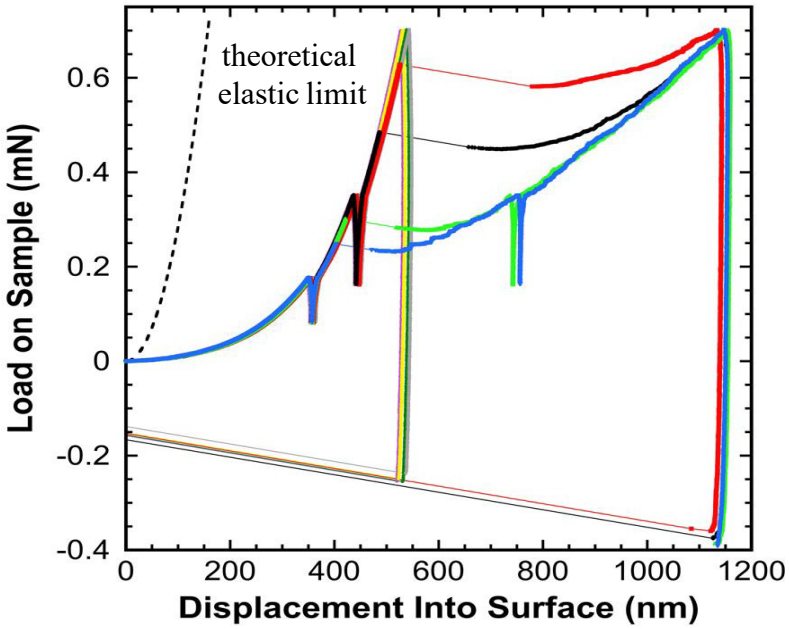

Figure 2.1. Representative cyclic load displacement curves in well- annealed, high purity indium at a homologous temperature of 0.69. The black dashed line represents the theoretical elastic load-displacement curve for the equivalent cone (centerline-to- face angle = 70.32°).

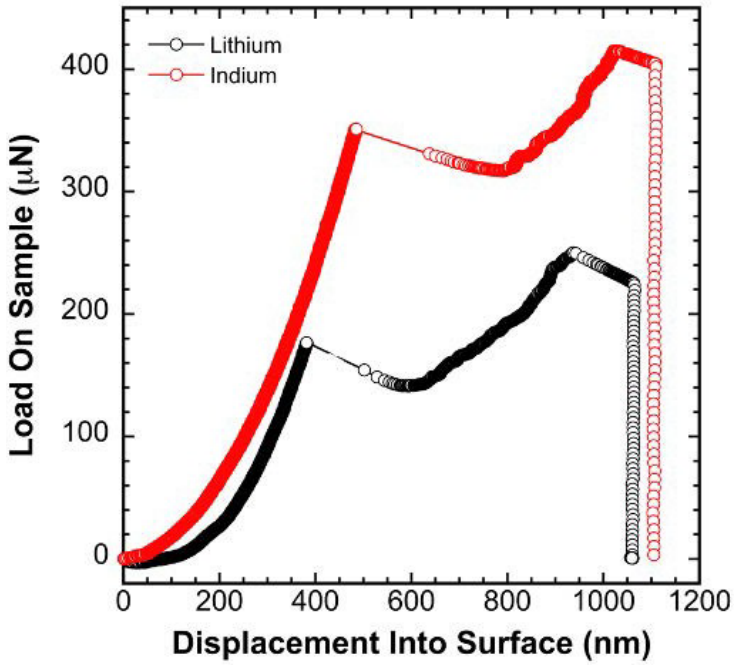

Figure 2.2. Representative load displacement curves in well- annealed, high purity indium and a high-purity, vapor deposited 18 μm thick lithium film.

Immediately prior to testing, the ~3 mm thick indium specimen was annealed in an evacuated quartz cylinder at a homologous temperature, T_H, of 0.89 for 6 hours. Post-test, energy dispersive x-ray spectroscopy (EDS) was performed immediately after imaging the residual hardness impressions and revealed no significant oxygen or carbon contamination on the free surface. Through etch pit analysis, the resulting dislocation density at the surface, ρ, was determined to be 7.09×10^4 cm^{-2}, which corresponds to an average dislocation spacing of $\rho^{-0.5} = 37.6$ μm. Figure 2.3 (a) shows representative etch pits in close proximity to the array of residual hardness impressions. In this well-annealed, low dislocation density condition, the $P-h$ curves are nominally expected to display a discernable strain burst or "pop-in" indicating the transition from elastic to elastic-plastic deformation [12]. Metallic specimens in a similar condition (well-annealed) frequently exhibit pop-ins at indentation depths ranging from ~10 to 200 nm [12]. The magnitude of the displacement burst often spans a similar range. Figure 2.3 (b), however, shows the $P-h$ curves are completely smooth and monotonically increasing to the first partial unload, giving no discernable evidence of the onset of plastic deformation. While an extremely sharp indenter tip could make the transition difficult to detect or perhaps even completely obscure it, the tip employed here is neither extremely sharp nor blunt. As shown in Figure 2.4, the projected area, A_p, given by a mathematical description of the indenter tip's physical geometry (the area function) is found to match the A_p of an infinitely sharp equivalent cone to within 10% or better only at contact depths ≥ ~200 nm. Given the well-annealed condition of the test specimen, the sharp but not too sharp indenter tip geometry and the high T_H, the absence of pop-ins suggests the plastic deformation mechanism prior to the observed strain bursts may not be shear driven dislocation glide, but rather a form of diffusive flow.

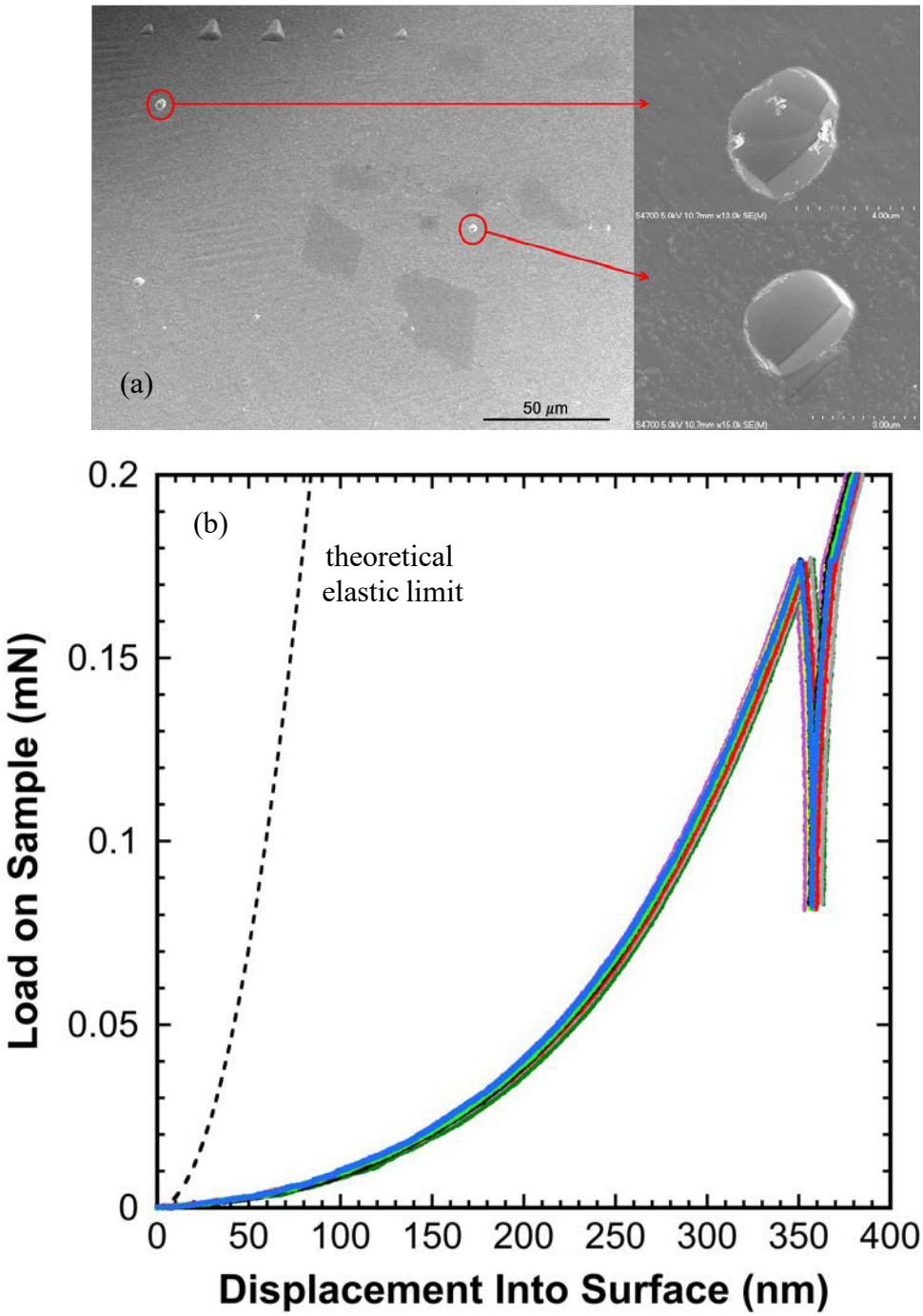

Figure 2.3. (a) Two representative etch pits and (b) eight representative load-displacement curves in indium, showing no evidence of the transition from elastic to elastic-plastic deformation (no pop-ins).

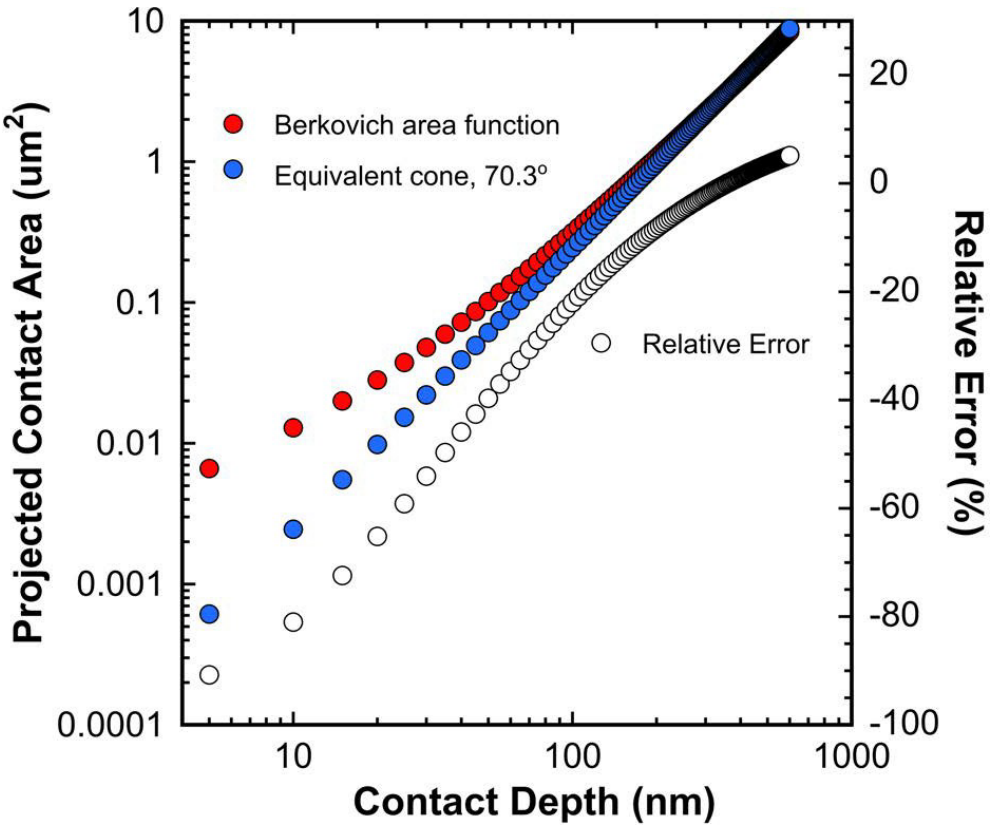

Figure 2.4. Direct comparison of the projected contact area between the Berkovich indenter tip's area function and an infinitely sharp equivalent cone.

Details regarding the significant amount of additional load required to pull the indenter tip off the surface of the test specimen are not well understood. Among the potential experimental artifacts that could systematically contribute to the apparent adhesion between the indium surface and the diamond indenter tip, several can justifiably be eliminated: (1) Uncertainty in the surface detection is minimal, as the zero point is accurate to within 5 nm or better; (2) Thermal drift is unlikely to be a significant source of error in the measured displacement because each individual experiment was performed in less than 60 seconds and the peak displacements are relatively large ($\geq$ 550 nm); (3) Uncertainty in the frame stiffness is also an unlikely source of significant error in the measured displacement because the relatively large flat-backed test specimen is rigidly mounted to a glass slide with a thin layer of epoxy and the estimated elastic contact stiffness at the peak displacement of 1200 nm is ~65 kN/m (assuming $E = 12.7$ GPa, the contact depth, $h_c =$

1200 nm, Poisson's ratio of indium, $\nu = 0.45$ & the projected contact area, $A_p = 13$ μm^2), which is only 6.1% of the measured frame stiffness (1.06×10^6 N/m).

2.4.2 Residual Hardness Impressions

Images from a scanning electron microscope (SEM) in Figure 2.5 show (a) the 5×5 array of residual hardness impressions in well-annealed, high purity indium, (b) a representative residual hardness impression from one of the six measurements exhibiting a strain burst (45° *y*-axis tilt), (c) a representative impression from one of the 19 measurements that do not exhibit a strain burst (45° *y*-axis tilt), and (d) a representative impression used to measure the projected contact area from a $P - h$ curve that did not exhibit a strain burst. The accuracy of the microscope's scale marker was experimentally verified using a single diffraction grating with 3 μm spacing as well as the 30 μm *x*-*y* spacing between the residual hardness impressions shown in Fig. 5 (a), which were placed by the instrument's piezo stages. In both cases, the measured distances were found to match the known values to within 3% or better.

Despite being subjected to the same maximum load and exhibiting indistinguishable $P - h$ curves prior to the strain burst, the SEM images and the corresponding $P - h$ data show the pop and no pop curves correlate to significantly different contact dimensions and strikingly different surface morphologies. As shown in Figure 2.5 (b), the $P - h$ curves exhibiting the pop create a larger contact and a surface morphology characterized by little to no discernable pile-up, straight, well-defined contact edges and distinct hemispherical slip traces in the free surface that appear as concentric rings radiating outward from 2 of the 3 faces of the residual hardness impression (plastic anisotropy). In contrast, Figure 2.5 (c) shows the no pop $P - h$ curves create a significantly smaller contact and result in a surface morphology characterized by significant pile-up, curved contact edges and no discernable slip traces in the free surface. This direct comparison between the pop and no pop residual hardness impressions and the corresponding $P - h$ curves clearly indicates a significant change in the stress relaxation mechanism operating before and after the strain burst. Furthermore, the characteristic features of the surface morphologies suggest the

volume of material displaced by the indenter tip during the no pop experiments may be uniquely conserved by the observed pile-up rather than the hinterland. In the analysis that follows, a new model is presented that rationalizes the observed pile-up based on interface diffusional flow.

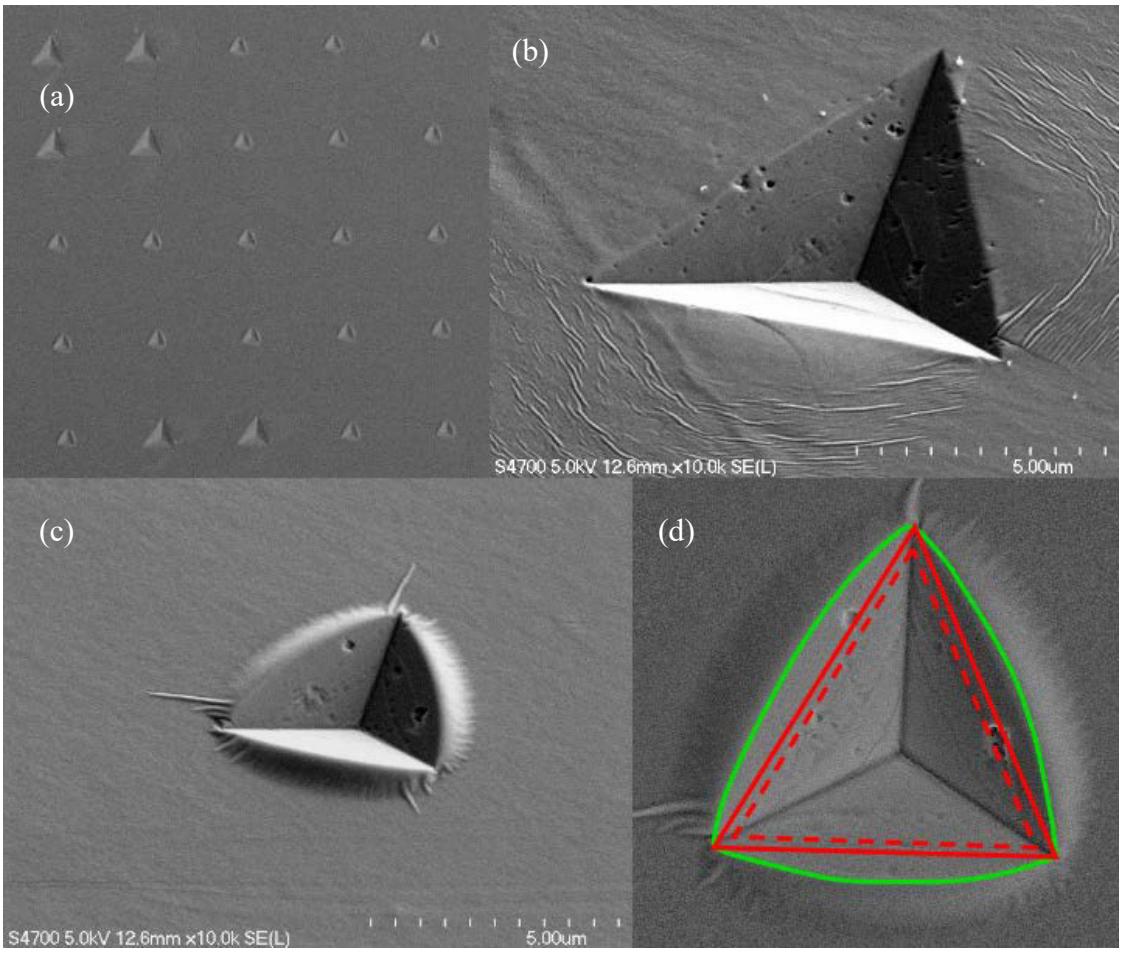

Figure 2.5. (a) The 5x5 array of residual hardness impressions. (b) and (c) show representative impressions from indents that do and do not, respectively, exhibit a strain burst. The y-axis of the microscope stage is rotated by 45°. (d) A representative illustration of the projected contact area. The dashed and solid red boundaries ignore pile-up and indicate the projected area based on the measured indentation depth and the residual impression, respectively. The solid green boundary shows the additional contact dimensions due to pile-up.

In addition to the EDS analysis, we further note that images of the residual hardness impressions in Figure 2.5 show no discernable evidence of cracking or spalling of an oxide

layer. After annealing for 6 hours at $T_H = 0.89$, the diffusion length was approximately 12 μm (D is given in Table I). Although the average grain size was not formally measured, many of the grains were within the range of 2 to 3 mm in diameter. As such, the entire 5×5 array of indents was performed near the center of a single grain, albeit with an unknown orientation. Assuming the important stress field beneath the indenter tip is constrained within a hemispherical radius that is 10 times the depth, then even at the maximum transition depth of 550 nm (10*0.55 μm = 5.5 μm), it is unlikely that prior to the indentation test, in its well-annealed condition, that the volume of indium to be sampled by the indenter encompassed a significant gradient in the dislocation density or residual stresses. Furthermore, if a uniform dislocation gradient did exist in the well-annealed condition, then presumably the $P - h$ data from indents within the same grain would generate a more repeatable pop-in depth from one test site to the next, not the stochastic response observed in Figure 2.1.

2.4.3 Hardness (the mean pressure the surface is capable of supporting)

Figure 2.6 (a) shows the measured hardness, H, ($H = P/A_p$) of well-annealed, high purity indium at a T_H of 0.69. In rationalizing this result, we consider the effect of pile-up, the depth dependence and the magnitude of the measured versus the nominally expected H. Capitalizing on indium's extremely high ratio of elastic modulus to yield strength, ~13,700 (Table I), the H data shown in Figure 2.6 (a) were calculated by intentionally ignoring the elastic deflection of the free surface and assuming that the contact depth, h_c, is accurately approximated by the indentation depth, h [2]. In other words, the H was calculated by assuming h_c is in the original plane of the surface. Based on the images of the residual hardness impressions, this simplifying assumption is clearly only valid at the maximum load, P_{max}, for the measurements that exhibit a strain burst, as they do not show any discernable evidence of pile-up or sink-in. For the measurements that do not exhibit a strain burst, an accurate estimate of H at P_{max} can only be obtained by accounting for the pile-

up through a direct a measurement of A_p from the unloaded residual hardness impression. Figure 2.5 (d) shows concentric outlines of three projected areas used in analyzing the $P-h$ curves that do not exhibit a strain burst. The outer most outline in green represents the A_p adjusted for pile-up. Once the pile-up is considered, the A_p at the indentation depth of 550 nm increases from 7.1 to 13.0 μm^2. Correspondingly, the peak H decreases by 48%, from ~103 to ~54 MPa. At the maximum depth of 1150 nm, the SEM image of the residual hardness impression, Figure 2.5 (b), shows no discernable evidence of pile-up or sink-in (the pile-up is presumably consumed by the strain burst). As expected, the A_p measured from the SEM image and the A_p determined by assuming $h_c = h$ are found to match within 10%. The reported H of ~24 MPa is, therefore, taken to be a reasonable estimate of the H or the mean pressure the surface is capable of supporting at $h = 1150$ nm.

At indentation depths large enough to avoid the well-documented indentation size effect, ISE, ($h \geq$ ~1 to 3 μm) the nominally expected H of a bulk, polycrystalline metal is ~3 times the metal's flow stress, σ_f, at the characteristic strain imposed by the indenter tip geometry (nominally 8% for the Berkovich) [12]. Given the high T_H of 0.69, the effect of work hardening is taken to be minimal and, thus, we assume $\sigma_f = \sigma_y$. As such, the nominally expected bulk $H = 3\sigma_y = 3(0.93 \text{ MPa}) = 2.8$ MPa. In comparison, the pile-up corrected peak H of ~54 MPa is nearly 20 times larger. Assuming the theoretical shear strength of indium lies within the range of $G/(2\pi)$ to $G/30$, where G is the shear modulus of indium ($G = 3.8$ GPa), we note 54 MPa is at most 43% of indium's theoretical shear strength.

While the peak H of ~54 MPa occurs at a depth ($h =$ ~550 nm) well within the expected intrinsic ISE window, we reject the ISE as a potential explanation for the difference between the measured and expected H. As previously noted, the high T_H, the low dislocation density, the lack of pop-ins in the $P-h$ curves, and the apparent frustration of dislocation mediated flow collectively suggest a dominant flow mechanism other than dislocation glide, which is a fundamental tenet of the ISE [12]. Nevertheless, neglecting these observations and assuming the deformation prior to the strain burst is mediated by

dislocation glide, then an intrinsic ISE would require a breakdown in geometric self-similarity of the contact such that the observed depth dependence prior to the strain burst is completely reversed. While not impossible, this scenario seems highly improbable.

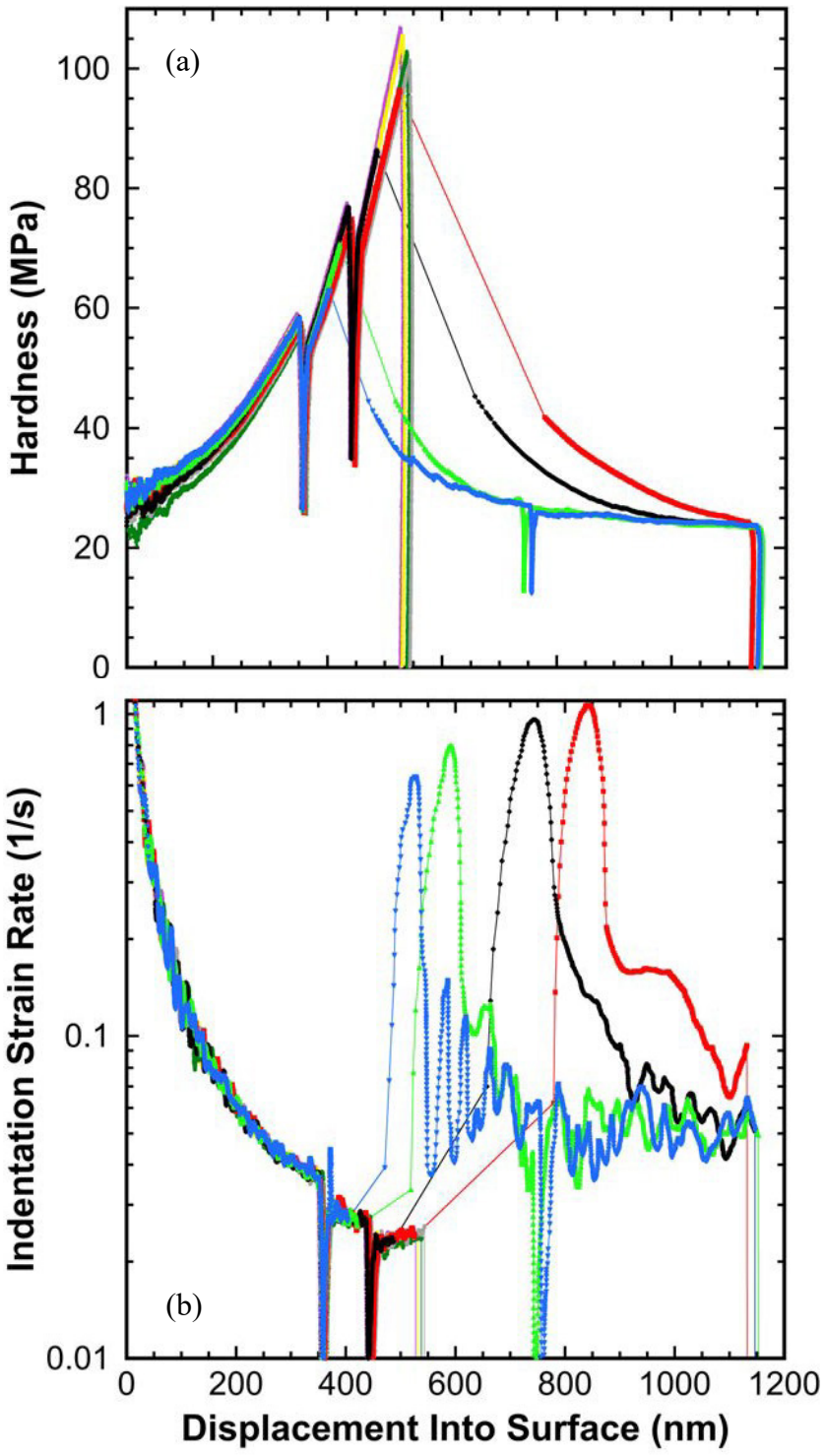

Figure 2.6. (a) The measured hardness as a function of depth. Direct comparison of the projected contact area between the Berkovich indenter tip's area function and an infinitely sharp equivalent cone.

An alternative explanation for the observed discrepancy between the measured and expected H is that plastic deformation prior to the observed strain burst is mediated by a less efficient flow mechanism such as stress directed diffusion rather than dislocation glide. In this context, the comparison between the measured H and $3\sigma_y$ is invalid. While models capable of predicting the measured H in terms of diffusional flow do exist, they are currently limited to volume diffusion [1-3]. As will be examined in a subsequent section, here we propose the dominant plastic deformation mechanism is interface rather than volume diffusion (both have a stress exponent, n, of 1) [2, 7, 8]. In the absence of a model that incorporates this mechanism and enables quantitative comparisons, here we qualitatively note that in comparison to dislocation glide, diffusive flow naturally depends on the diffusion length and, therefore, becomes an increasingly less efficient stress relaxation mechanism as the diffusion length increases with indentation depth [2, 6, 7]. We also note that within the limit of diffusional flow, it is possible that geometric self-similarity of the contact is not lost. Although clearly speculative, this outcome would potentially provide a simple means of accounting for pile-up and correcting the nominally measured H as a continuous function of depth. In this way, the measured H at $h \leq 550$ nm would be uniformly decreased by 48%, noting, however, that potential strain rate effects have not been considered. While elucidating rate effects is clearly a necessary and critical step forward, it is important to understand that conventional constant strain rate nanoindentation loading algorithms, such as the $\dot{P}/P$ technique used here, by definition, cannot generate a constant strain rate at any length scale wherein the hardness is depth dependent. To that end, unambiguous examination of the competing effects of length scale and strain rate await the development of novel testing methods that are capable of controlling and maintaining a constant indentation strain rate under the unique stress directed diffusional flow conditions observed here.

As previously reported, the H of ~24 MPa at the maximum depth of 1150 nm is taken to be an accurate estimate of the mean pressure the surface is capable of supporting. Although the deformation at this depth is presumably dominated by dislocation glide, we note the measured H is still 8.6 times larger than the nominally expected $3\sigma_y = 2.8$ MPa (a constraint factor of nearly 26 rather than the expected value of 3). Among the factors

potentially contributing to this discrepancy are an intrinsic ISE and strain rate sensitivity. Following an idea first proposed by Rester et al., it is also possible that following the transition or pop-in, dynamic recrystallization enables geometrically necessary dislocations (brought about by the gradient in strain directly beneath the indenter tip) to coalesce into cell walls or subgrains, thus providing an additional strengthening mechanism [11]. Although the T_H of 0.69 is well within the hot working regime, it is also plausible that our assumption of negligible work hardening immediately following the burst is inaccurate. Indium's self-diffusion coefficient is quite small and, therefore, it is not clear how efficient or inefficient the recovery process is over the time scale from the strain burst to the maximum load ($\leq$ 20 s). The potential effect of strain rate is difficult to quantify, as indium's strain rate sensitivity at these length scales and under diffusional flow is entirely unknown [13, 14]. For the sake of posterity, Figure 2.6 (b) shows the depth dependent indentation strain rate, defined as the time rate of change of the displacement divided by the displacement, $\dot{h}/h$. Over the indentation depths examined here, Figure 2.6 (b) shows the strain rate spans nearly two orders of magnitude, from $\sim$1 to 0.02 s^{-1}. We note the peak strain rate following the burst is an underestimation, as the calculated velocity utilizes an effective time constant of $\sim$0.2 s.

Due to the small number of measurements (25 test sites), rigorous analysis of the stochastic nature of the strain burst is beyond the scope of this investigation. However, based on the striking similarities between the $P-h$ behavior of indium and lithium shown in Figure 2.1(b), here we adopt the same rationalization of the strain burst. Specifically, the strain burst is taken to represent an abrupt transition from diffusion to dislocation mediated flow. Given the stochastic nature of the transition and the low dislocation density, we speculate that the sudden event is triggered by the combination of a critical threshold in stress and a sufficient length scale, as the dislocation mechanism clearly appears to require not only the necessary driving force, but sufficient room to physically operate [2].

2.4.4 Volume Versus Interface Diffusion

Enabled by a high T_H and a low dislocation density, we submit that diffusive flow is the most efficient stress relaxation mechanism at length scales that are small in relation to the spacing between mobile dislocations and/or operable dislocation multiplication sources. As presented in Table 2.1, indium's self-diffusion coefficient, D, at the test temperature of 24.4 °C is 5.7×10^{-18} m^2/s. This coefficient is quite small and suggests that volume diffusion to the free surface may not be an efficient transport mechanism, particularly as the diffusion length increases with indentation depth. Interface diffusion, on the other hand, requires approximately 1/2 to 2/3 the activation energy of volume diffusion. Assuming $Q_{d\ interface} = Q_{d\ volume}/2$, then the corresponding interface diffusion coefficient is 4.29×10^{-11} m^2/s. Here we assume the interface diffusion layer is 0.5 nm thick and that the relevant interface volume is the product of the thickness and the interface surface area under pressure. At an indentation depth of 550 nm, previous analysis indicates the interface volume fraction is 6.62×10^{-5} [2]. The effective diffusion coefficient given by Tilley is

$$D_{effective} = (1 - f)D_{volume} + fD_{interface} \tag{2.1}$$

and, thus, $D_{effective} = 2.8 \times 10^{-15}$ m^2/s, which is three orders of magnitude larger than volume diffusion alone [15]. Alternatively, if the ratio is only 2/3, $D_{effective}$ is still more than an order of magnitude larger. This simple analysis indicates the diffusive flow mechanism for indium at 24.4 °C is dominated by interface rather than volume diffusion. For the sake of comparison, we note the opposite is true of lithium at a similar temperature. Even at a substantially smaller depth, 150 nm, the interface term is found to contribute only 4% to the effective diffusion coefficient. As indicated in Table I, the apparent explanation for this difference is lithium's self-diffusion coefficient, which is nearly three orders of magnitude larger than that of indium.

2.4.5 Quantifying the Observed Pile-Up

To create a two-dimensional profile of the pile-up, a line scan performed in the SEM was used to deposit a thin line of carbon through a residual hardness impression. By aligning the carbon line with the *y*-axis of the SEM stages and then tilting the *y*-axis by 45°, direct measurements of the $x - y$ coordinates of the carbon line were used to estimate the pile-up profile. While a properly calibrated atomic force microscope could presumably simplify this task, one was not readily available. Figure 2.7 shows the line scan oriented along the *y*-axis and tilted by 45°. The measured pileup profile is shown in Figure 2.7 (b).

Based on the recorded $P - h$ data and measurements from the SEM images of the in-plane dimensions of the residual hardness impressions and the pile-up profile, Figure 2.8 (a) shows a two-dimensional rendering of the contact geometry relative to the original plane of the surface. To capture key features of the geometry, the image presents an overlay that combines elements from three different cross-sections through (1) the center of an indent, (2) along an edge (corner-to-corner) and (3) along the ridge of the pile-up (corner-to-corner). The color coding corresponds to the residual hardness impression shown in Figure 2.5 (d). In an attempt to compensate for the off-center line scan, the peak pile-up height at the center of the face was estimated by fitting a parabola to the three points indicated along the ridge of the pile-up. As measured in the SEM, the average side length (corner-to-corner) and the position of the carbon line from the furthest corner were found to be 4.6 μm $\pm$ 4.9% and 3.45 μm, respectively. As per the parabolic fit, the peak pile-up height at the center of the face is estimated to be 229.0 nm, which is ~22.5% larger than the profile height measured from the line scan. Among the interesting observations, we note the A_p calculated by the indenter tip's area function at $h = 550$ nm underestimates the measured A_p (assuming no pile-up) by 21%. Based on the elevated corners (relative to the original plane of the surface) of the residual impressions shown in Figures 2.5 (c) and 2.7 (a), we propose this outcome is due to the flow of indium along the faces and below the corners of the indenter tip. In this way, the complete triangular residual hardness impression can physically climb above the original plane of the surface as depicted in Figure 2.8 (a). In

other words, we submit the pile-up is not limited to occurring only along the faces of the indenter tip, as one might intuitively expect.

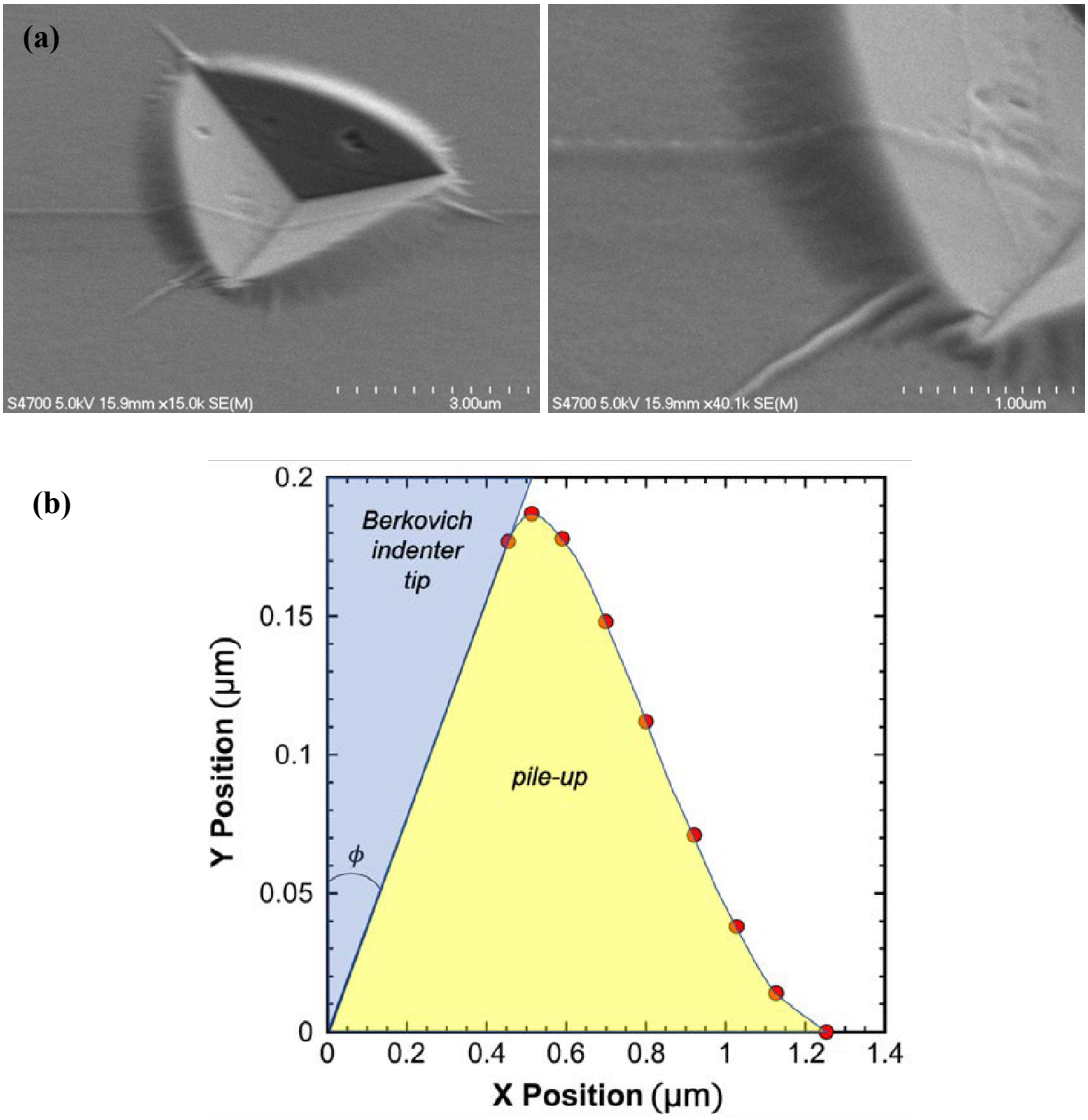

Figure 2.7. (a) The deposited carbon (line scan) through a residual hardness impression. The y-axis of the microscope stage is aligned parallel with the carbon line and tilted by 45°. (b) The measured pile-up profile as determined by measuring the x-y coordinates of the carbon line.

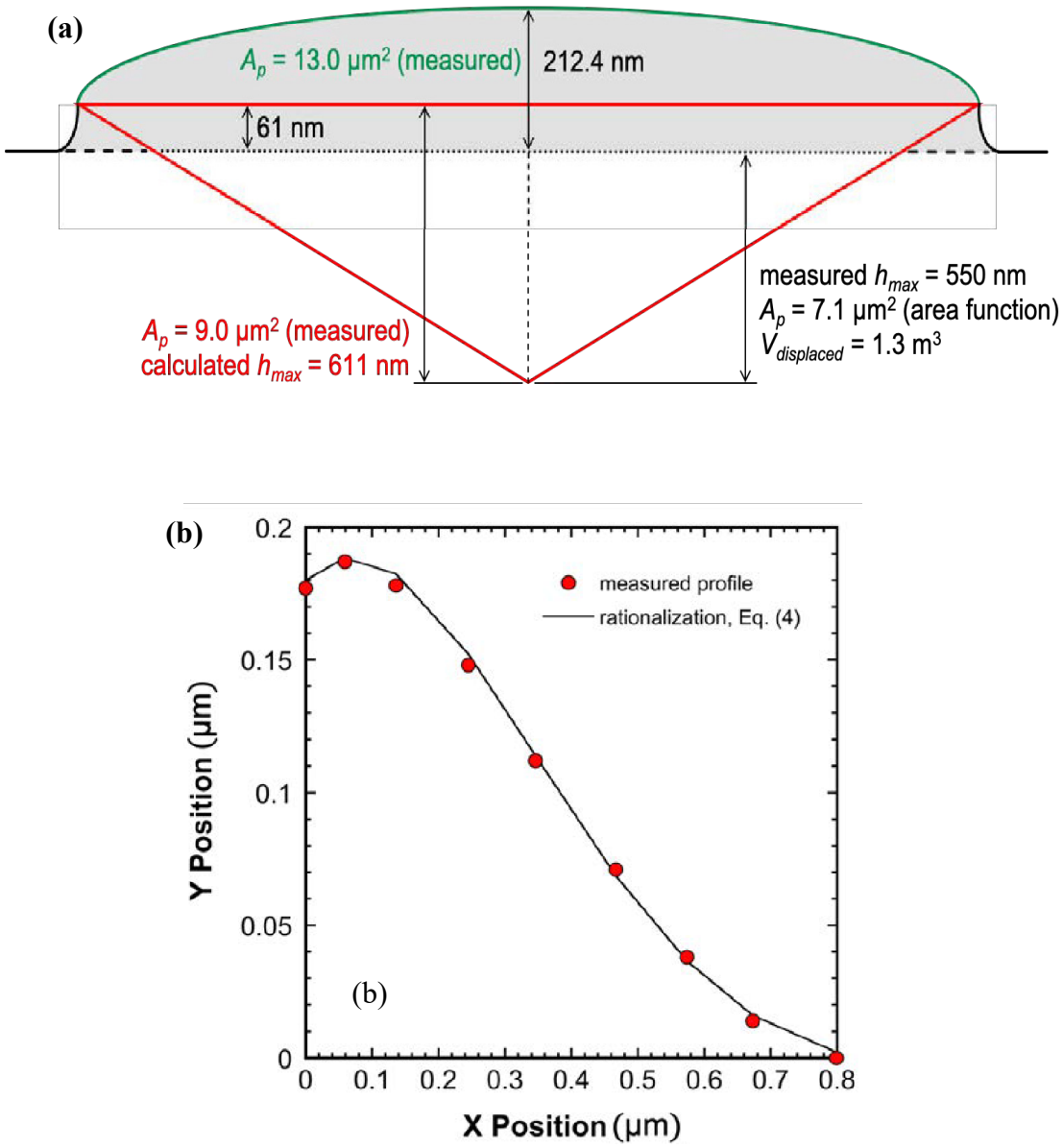

Figure 2.8. (a) A two-dimensional rendering of the contact geometry based on an overlay of three cross-sections through (1) the center of an indent, (2) along an edge (corner-to-corner), and (3) along the peak of the pile-up (corner-to-corner). (b) Rationalization of the pile-up profile using Eq. (2.5), which is based on interface diffusion.

2.4.6 A Simple Look at Conservation of Volume

If the proposed stress relaxation mechanism is interface diffusion, then the volume of indium displaced by the indenter tip must be locally conserved by the pile-up. Limited by a single profile of the pile-up, our analysis is constrained to a rudimentary examination of the pile-up volume. As indicated by Figure 2.8 (a), the volume of indium displaced by the indenter tip relative to the original plane of the surface is 1.3 μm^3. As described above, here we assume the ridge of the pile-up is reasonably approximated by the parabola $y = 0.061 + 0.14609x - 0.031758x^2$, where y and x are in units of μm and physically represent the height of the pile-up relative to the original plane of the surface and the horizontal position along the face, respectively. At the position of the line scan ($x = 3.45$ μm as measured in the SEM), the radius of a circle whose area is equivalent to the area under the profile is found to be 0.196 μm. Thus, the ratio of the pile-up height to equivalent radius is 0.955. Assuming that ratio is constant over the side length of the residual hardness impression, then the volume of the pile-up along all three faces is given by the definite integral,

$$V_{pile-up} = 3\pi \int_0^{4.6} (0.063893 + 0.15302x - 0.033264x^2)^2 \, dx \tag{2.2}$$

where the limits correspond to the average corner-to-corner side length and the integrand gives the equivalent radius as a function of position (x) along each face. In this way, the estimated volume of the pile-up is found to be 1.54 μm^3, which compares reasonably well with the displaced volume of 1.3 μm^3 (the relative error is 18.5%). This analysis demonstrates the distinct possibility that the displaced volume is uniquely conserved by the pile-up.

2.4.6.1 Rationalizing the Pile-Up via Interface Diffusion

Interface diffusion along the faces of the indenter tip will be driven by gradients in the chemical potential at the free surface of the indium and at the interface between the indenter and the indium. For diffusion at the free surface, it is considered that the chemical potential, μ (J/kg), is a function of both the surface strain energy, $\sigma^2/2E$, and the surface curvature, κ (1/m), where σ is the stress at the free surface (normal components are null) and E is the elastic modulus [16]. This may be written as

$$\mu = \mu_o + \frac{\sigma^2 \Omega}{2E} - \Omega\gamma\kappa \tag{2.3}$$

where Ω (m^3/atom) is the atomic volume and γ (J/m^2) is the surface energy.

Here we use a quasi-steady state solution to describe the surface profile motivated by Mullins, where the surface profile depends on a constant (or slowly changing) triple point velocity, V [17]. The original treatment by Mullins described a quasi-steady state profile for a moving grain boundary-surface triple junction, which is modified here to apply to the triple junction of the indenter-indium interface, indium surface and vapor phase with inclusion of the elastic strain energy term. From this approach, the surface profile, $y(x)$, is obtained from the solution of the differential equation

$$0 = \frac{D_s \delta \Omega}{k_B T}\left(\frac{H^2}{E}\omega^2 \exp(-\omega x) - \gamma \frac{d^4 y}{dx^4}\right) + V\frac{dy}{dx} \tag{2.4}$$

where x is the horizontal surface position in a moving coordinate system of velocity, V, which is the triple point velocity with the indenter/indium triple point at the origin, D_s (m^2/s) is the surface diffusivity, δ is the surface layer thickness, H is the hardness, T is the

temperature, k_B is the Boltzmann constant, and $1/\omega$ is a relaxation length for the elastic stress. A general solution to Eq. (2.4) is of the form

$$y = C\exp(-\omega x) + A\exp\left(-\frac{\lambda x}{2}\right)\cos\left(\frac{\sqrt{3}}{2}\lambda x\right) + B\exp\left(-\frac{\lambda x}{2}\right)\sin\left(\frac{\sqrt{3}}{2}\lambda x\right) \quad (2.5)$$

The substitution of Eq. (2.5) into Eq. (2.4) defines the coefficients C and λ in terms of physical parameters. Grouping the parameters into a and b gives

$$a\,(-) = \frac{H^2\omega^2}{E}\frac{D_s\delta\Omega}{k_BTV} \quad (2.6)$$

$$b\,(\mathrm{m}^3) = \frac{\gamma D_s\delta\Omega}{k_BTV} \quad (2.7)$$

The parameters of C and λ can be then determined as

$$C\,(\mathrm{m}) = \frac{a}{b\omega^4 + \omega} \quad (2.8)$$

$$\lambda\,(\mathrm{m}^{-1}) = \left(\frac{1}{b}\right)^{\frac{1}{3}} \quad (2.9)$$

where ω is the inverse of the indentation depth (based on the Saint-Venant principle). Using the carbon line profile presented in Figure 2.7 (b), Eq. (2.5) can be fit to the indium pile-up profile as shown in Figure 2.8 (b). Admittedly, there are a large number of fitting parameters available to produce the close fit shown in Figure 2.8 (b), but as discussed above, Eqs. (2.6)-(2.9) provide a physical basis for three (ω, C and λ) of the five fitting parameters. A comparison of the fitting parameter values against the estimated values is shown in Tables 2.1 and 2.2, where the parameters are found to be within an order of magnitude with respect to the physical estimates.

Table 2.2. Comparison of the physical estimates and fitting parameters.

Parameter	Physical Estimate	Fitting Parameter
a (-)	0.01	NA
b (m^3)	3.17×10^{-20}	NA
C (m)	8.27×10^{-9}	6.0×10^{-8}
λ (1/m)	3.16×10^{6}	4.7×10^{6}
ω (1/m)	1.2×10^{6}	1.2×10^{6}
A (m)	NA	1.2×10^{-7}
B (m)	NA	1.5×10^{-7}

In future studies, the proposed rationalization provides a unique opportunity to examine geometric self-similarity as well as the functional relationship between the measured properties, the contact dimensions and the mechanism(s) of plastic deformation. Of particular interest are the effects of temperature, strain rate and indenter tip geometry. Collectively, the rationalization proposed here and the existing $P - h$ relationships based on volume diffusion provide an extensive framework capable of providing new insight into small length scale creep mechanisms and the conditions that inhibit and/or promote the formation and growth of metallic filaments or dendrites originating at the interface between a metallic anode and a solid electrolyte separator.

2.5 Summary and Conclusions

Nanoindentation in well-annealed, high purity indium was performed under the following conditions: Berkovich indenter tip, cyclic loading that was terminated at 175, 350 and 700 μN, load control such that the loading rate divided by the load was targeted at 0.1 s^{-1}, measured indentation strain rates varying from 0.02 to 1 s^{-1}, and a homologous temperature of 0.69 (24.4 ºC).

(1) The load–displacement curves and corresponding residual hardness impressions show the plastic deformation mechanism varies significantly with indentation depth and test

site. Among 25 indents, 19 (76%) reach the peak load of 700 μN with no discontinuity in the measured load-displacement curve. The corresponding residual hardness impressions are characterized by bowed contact edges, significant pile-up and no discernable slip traces around the periphery of the contact. Despite being terminated at the same maximum load, the remaining 6 indents (24%) experience a stochastic strain burst and form a residual hardness impression that is approximately twice as deep, characterized by well defined, straight contact edges, no discernable pile-up and slip traces in the free surface around 2 of the 3 indenter faces. Based on these observations and the estimated dislocation spacing of 37.6 mm, we submit the strain burst represents an abrupt transition from interface diffusion to dislocation mediated flow. Given the stochastic nature of the transition and the low dislocation density, we speculate that the sudden event is triggered by the combination of a critical threshold in stress and a sufficient length scale, as the dislocation mechanism clearly appears to require not only the necessary driving force, but sufficient room to physically operate.

(2) At the peak load of 700 μN, 19 of 25 targeted test sites (76%) did not experience a strain burst, terminated at a depth of ~550 nm and yielded a measured hardness (pile-up corrected) of ~54 MPa. The remaining 6 test sites (24%) did experience a strain burst, terminated at a depth of ~1150 nm and yielded a measured hardness of ~24 MPa (no pile-up or sink-in correction was deemed necessary). Based on the substantially higher hardness and extensive pile-up indicative of the test sites that do not experience a strain burst, we propose the dominant stress relaxation mechanism prior to the strain burst is interface diffusion rather than dislocation mediated glide. Interface rather than volume diffusion is favored because the effective interface diffusion coefficient is 1 to 3 orders of magnitude larger than volume diffusion alone. Although the analysis is rudimentary, the estimated pile-up volume is found to be within 18.5% of the volume of indium displaced by the indenter tip. This suggests the plastically deformed volume of material may be uniquely conserved by the pile-up.

(3) The measured pile-up profile is rationalized using a new analytical model based on interface diffusion. The model is derived from Mullins' analysis of a moving grain

boundary. Among the model's 5 fitting parameters, 3 are defined in terms of material or experimental parameters. This model, in conjunction with previously derived volume diffusion load-displacement relationships, expands the analytical framework to examine small length scale creep mechanisms. This capability will serve to develop new insight into the stress relaxation mechanisms operating at the interface between a metallic anode and a solid electrolyte separator.

2.6 Acknowledgements

This research was sponsored jointly by the U.S. Department of Energy, Office of Energy Efficiency and Renewable Energy's Advanced Battery Materials Research program (managed by Tien Duong), and by TARDEC, the U.S. Army Tank Automotive Research Development and Engineering Center. EGH and PSP were also partially supported by the Indo-U.S. Science & Technology Forum (IUSSTF) through the Virtual Networked Center award JC-045/2018. EGH is also particularly grateful for start-up funding from the Department of Materials Science and Engineering at Michigan Technological University.

2.7 References

1. Herbert, E.G., et al., *On the mechanisms of stress relaxation and intensification at the lithium/solid-state electrolyte interface.* J. Mater. Res., 2019. **34**(21): p. 3593-3616.
2. Herbert, E.G., et al., *Nanoindentation of high purity vapor deposited lithium films: A mechanistic rationalization of diffusion-mediated flow.* J. Mater. Res., 2018. **33**(10): p. 1347-1360.
3. Herbert, E.G., et al., *Nanoindentation of high purity vapor deposited lithium films: A mechanistic rationalization of the transition from diffusion to dislocation-mediated flow.* J. Mater. Res., 2018. **33**(10): p. 1361-1368.
4. Chung, Y. and C. Lee, *Electrochemical behaviors of Indium.* Journal of Electrochemical Science and Technology, 2012. **3**(1): p. 1-13.
5. Ashby, M., *CES EduPack.* Granta Design, 2019.
6. Feng, G. and A. Ngan, *Creep and strain burst in indium and aluminium during nanoindentation.* Scripta materialia, 2001. **45**(8): p. 971-976.
7. Li, H. and A. Ngan, *Size effects of nanoindentation creep.* Journal of Materials Research, 2004. **19**(2): p. 513-522.
8. Li, W. and R. Warren, *A model for nano-indentation creep.* Acta metallurgica et materialia, 1993. **41**(10): p. 3065-3069.
9. Han, B.Q. and T.G. Langdon, *Factors contributing to creep strengthening in discontinuously-reinforced materials.* Materials Science and Engineering: A, 2002. **322**(1-2): p. 73-78.
10. Fincher, C., et al., *Elastic and Plastic Characteristics of Sodium Metal.* ACS Appl. Energy Mater. , 2020. **3**(3): p. 1759-1767.
11. Rester, M., C. Motz, and R. Pippan, *Microstructural investigation of the volume beneath nanoindentations in copper.* Acta Materialia. **55**(19): p. 6427-6435.
12. Pharr, G.M., E.G. Herbert, and Y.F. Gao, *The indentation size effect: A critical examination of experimental observations and mechanistic interpretations.* Ann. Rev. Mat. Res., 2010. **40**: p. 271-292.
13. Lucas, B.N., *An Experimental Investigation of creep and Viscoelastic Properties Using Depth-Sensing Indentation Techniques*, in *Materials Science and Engineering*. 1997, University of Tennessee.
14. Lucas, B. and W. Oliver, *Indentation power-law creep of high-purity indium.* Metallurgical and materials Transactions A, 1999. **30**(3): p. 601-610.
15. Tilly, R., *Defects in Solids*. Vol. 244. 2008, Hoboken, New Jersey, USA: John Wiley and Sons.
16. Asaro, R. and W. Tiller, *Interface morphology development during stress corrosion cracking: Part I. Via surface diffusion.* Metallurgical and Materials Transactions B, 1972.
17. Mullins, W., *The Effect of Thermal Grooving on Grain Boundary Motion.* Acta Met, 1958. **6**(414).

A Appendix 2.A. Reprint Copyright Permission

SPRINGER NATURE LICENSE
TERMS AND CONDITIONS

Aug 08, 2022

This Agreement between Michigan Tech University -- Fereshteh Mallakpour ("You") and Springer Nature ("Springer Nature") consists of your license details and the terms and conditions provided by Springer Nature and Copyright Clearance Center.

License Number	5364290511167
License date	Aug 08, 2022
Licensed Content Publisher	Springer Nature
Licensed Content Publication	Journal of Materials Research
Licensed Content Title	Length-scale-dependent stress relief mechanisms in indium at high homologous temperatures
Licensed Content Author	Fereshteh Mallakpour et al
Licensed Content Date	Apr 14, 2021
Type of Use	Thesis/Dissertation
Requestor type	academic/university or research institute
Format	print and electronic
Portion	full article/chapter
Will you be translating?	no

Circulation/distribution	50000 or greater
Author of this Springer Nature content	yes
Title	LENGTH SCALE-DEPENDENT STRESS RELIEF MECHANISMS IN HIGH PURITY INDIUM
Institution name	Michigan Technological University
Expected presentation date	Aug 2022
Requestor Location	Michigan Tech University 1400 Townsend Dr. HOUGHTON, MI 49931 United States Attn: Michigan Tech University
Total	0.00 USD

Terms and Conditions

Springer Nature Customer Service Centre GmbH
Terms and Conditions

This agreement sets out the terms and conditions of the licence (the **Licence**) between you and **Springer Nature Customer Service Centre GmbH** (the **Licensor**). By clicking 'accept' and completing the transaction for the material (**Licensed Material**), you also confirm your acceptance of these terms and conditions.

1. Grant of License

1. 1. The Licensor grants you a personal, non-exclusive, non-transferable, world-wide licence to reproduce the Licensed Material for the purpose specified in your order only. Licences are granted for the specific use requested in the order and for no other use, subject to the conditions below.

1. 2. The Licensor warrants that it has, to the best of its knowledge, the rights to license reuse of the Licensed Material. However, you should ensure that the material you are requesting is original to the Licensor and does not carry the copyright of another entity (as credited in the published version).

1. 3. If the credit line on any part of the material you have requested indicates that it was reprinted or adapted with permission from another source, then you should also seek permission from that source to reuse the material.

2. Scope of Licence

2. 1. You may only use the Licensed Content in the manner and to the extent permitted by these Ts&Cs and any applicable laws.

2. 2. A separate licence may be required for any additional use of the Licensed Material, e.g. where a licence has been purchased for print only use, separate permission must be obtained for electronic re-use. Similarly, a licence is only valid in the language selected and does not apply for editions in other languages unless additional translation rights have been granted separately in the licence. Any content owned by third parties are expressly excluded from the licence.

2. 3. Similarly, rights for additional components such as custom editions and derivatives require additional permission and may be subject to an additional fee. Please apply to Journalpermissions@springernature.com/bookpermissions@springernature.com for these rights.

2. 4. Where permission has been granted **free of charge** for material in print, permission may also be granted for any electronic version of that work, provided that the material is incidental to your work as a whole and that the electronic version is essentially equivalent to, or substitutes for, the print version.

2. 5. An alternative scope of licence may apply to signatories of the STM Permissions Guidelines, as amended from time to time.

3. Duration of Licence

3. 1. A licence for is valid from the date of purchase ('Licence Date') at the end of the relevant period in the below table:

Scope of Licence	Duration of Licence
Post on a website	12 months
Presentations	12 months
Books and journals	Lifetime of the edition in the language purchased

4. Acknowledgement

4. 1. The Licensor's permission must be acknowledged next to the Licenced Material in print. In electronic form, this acknowledgement must be visible at the same time as the figures/tables/illustrations or abstract, and must be hyperlinked to the journal/book's homepage. Our required acknowledgement format is in the Appendix below.

5. Restrictions on use

5. 1. Use of the Licensed Material may be permitted for incidental promotional use and minor editing privileges e.g. minor adaptations of single figures, changes of format, colour and/or style where the adaptation is credited as set out in Appendix 1 below. Any other changes including but not limited to, cropping, adapting, omitting material that affect the meaning, intention or moral rights of the author are strictly prohibited.

5. 2. You must not use any Licensed Material as part of any design or trademark.

5. 3. Licensed Material may be used in Open Access Publications (OAP) before publication by Springer Nature, but any Licensed Material must be removed from OAP sites prior to final publication.

6. Ownership of Rights

6. 1. Licensed Material remains the property of either Licensor or the relevant third party and any rights not explicitly granted herein are expressly reserved.

7. Warranty

IN NO EVENT SHALL LICENSOR BE LIABLE TO YOU OR ANY OTHER PARTY OR ANY OTHER PERSON OR FOR ANY SPECIAL, CONSEQUENTIAL, INCIDENTAL OR INDIRECT DAMAGES, HOWEVER CAUSED, ARISING OUT OF OR IN CONNECTION WITH THE DOWNLOADING, VIEWING OR USE OF THE MATERIALS REGARDLESS OF THE FORM OF ACTION, WHETHER FOR BREACH OF CONTRACT, BREACH OF WARRANTY, TORT, NEGLIGENCE, INFRINGEMENT OR OTHERWISE (INCLUDING, WITHOUT LIMITATION, DAMAGES BASED ON LOSS OF PROFITS, DATA, FILES, USE, BUSINESS OPPORTUNITY OR CLAIMS OF THIRD PARTIES), AND
WHETHER OR NOT THE PARTY HAS BEEN ADVISED OF THE POSSIBILITY OF SUCH DAMAGES. THIS LIMITATION SHALL APPLY NOTWITHSTANDING ANY FAILURE OF ESSENTIAL PURPOSE OF ANY LIMITED REMEDY PROVIDED HEREIN.

8. Limitations

8. 1. ***BOOKS ONLY:*** Where **'reuse in a dissertation/thesis'** has been selected the following terms apply: Print rights of the final author's accepted manuscript (for clarity, NOT the published version) for up to 100 copies, electronic rights for use only on a personal website or institutional repository as defined by the Sherpa guideline (www.sherpa.ac.uk/romeo/).

8. 2. For content reuse requests that qualify for permission under the STM Permissions Guidelines, which may be updated from time to time, the STM Permissions Guidelines supersede the terms and conditions contained in this licence.

9. Termination and Cancellation

9. 1. Licences will expire after the period shown in Clause 3 (above).

9. 2. Licensee reserves the right to terminate the Licence in the event that payment is not received in full or if there has been a breach of this agreement by you.

Appendix 1 — Acknowledgements:

For Journal Content:
Reprinted by permission from [**the Licensor**]: [**Journal Publisher** (e.g. Nature/Springer/Palgrave)] [**JOURNAL NAME**] [**REFERENCE CITATION** (Article name, Author(s) Name), [**COPYRIGHT**] (year of publication)

For **Advance Online Publication papers:**
Reprinted by permission from [**the Licensor**]: [**Journal Publisher** (e.g. Nature/Springer/Palgrave)] [**JOURNAL NAME**] [**REFERENCE CITATION** (Article name, Author(s) Name), [**COPYRIGHT**] (year of publication), advance online publication, day month year (doi: 10.1038/sj.[JOURNAL ACRONYM].)

For Adaptations/Translations:
Adapted/Translated by permission from [**the Licensor**]: [**Journal Publisher** (e.g. Nature/Springer/Palgrave)] [**JOURNAL NAME**] [**REFERENCE CITATION** (Article name, Author(s) Name), [**COPYRIGHT**] (year of publication)

Note: For any republication from the British Journal of Cancer, the following credit line style applies:

Reprinted/adapted/translated by permission from [**the Licensor**]: on behalf of Cancer Research UK: : [**Journal Publisher** (e.g. Nature/Springer/Palgrave)] [**JOURNAL NAME**] [**REFERENCE CITATION** (Article name, Author(s) Name), [**COPYRIGHT**] (year of publication)

For **Advance Online Publication** papers:
Reprinted by permission from The [**the Licensor**]: on behalf of Cancer Research UK: [**Journal Publisher** (e.g. Nature/Springer/Palgrave)] [**JOURNAL NAME**] [**REFERENCE CITATION** (Article name, Author(s) Name), [**COPYRIGHT**] (year of publication), advance online publication, day month year (doi: 10.1038/sj.[JOURNAL ACRONYM])

For Book content:
Reprinted/adapted by permission from [**the Licensor**]: [**Book Publisher** (e.g. Palgrave Macmillan, Springer etc) [**Book Title**] by [**Book author**(s)] [**COPYRIGHT**] (year of publication)

Other Conditions:

Version 1.3

Questions? customercare@copyright.com or +1-855-239-3415 (toll free in the US) or +1-978-646-2777.

3 Chapter 3: On the correlation Between the Stress Exponent for Creep Determined by Nanoindentation and the Mechanism of Action Enabling Stress Relief in Indium

To be submitted for publication.

3.1 Abstract

Instrumented indentation performed at room temperature with a Berkovich and 10 μm radius sphere has been used to measure the stress exponent for creep before and after the strain burst observed in well-annealed, high-purity indium. Before the strain burst, the measured values are successfully rationalized using a new model based on stress directed diffusional flow along the interface between the indenter tip and test specimen. After the strain burst, the measured stress exponents are found to be representative of dislocation glide and climb assisted glide. These results are compared and contrasted to the previous experimental investigations and modeling efforts of Feng et *al*., Lucas et *al*., and Li et *al*. Collectively, the experimental observations and rationalization presented here provide significant new insight into the mechanisms of action that control the competition for stress relief in small, constrained volumes of crystalline metals subjected to high homologous temperatures.

3.2 Introduction

By measuring the stress exponent for creep, n, using nanoindentation, the aim of this work is to elucidate the effect(s) of length scale on the stress relief mechanism(s) operating within small, constrained volumes of crystalline metals subjected to a high homologous temperature. In particular, our goal is to identify the dominant stress relief mechanism(s) operating before and after the well documented strain burst observed in high-purity, well-

annealed indium (see Figures 3.1 (b) and (d)) [1, 2]. In doing so, the intent is to provide new insight into the stress relief mechanisms that control the length-scale dependent competition for stress relief previously documented in high purity indium and lithium [2-4]. It is hoped that this knowledge will further support the development of next generation solid-state battery (SSB) materials capable of providing nominally stress-free, planar plating and stripping of a Li anode.

Over the past 5 years, significant advancements have been made in understanding the formation and growth of Li filaments or dendrites originating at the buried interface between a pure metallic Li anode and a solid electrolyte separator (SSE) [5]. Key among these advancements is a better understanding of the critical role mechanics plays in maintaining a stable and coherent interface during cycling of a cell. Through extensive examinations of Li's mechanical behavior at battery relevant length scales (dimensions commensurate with morphological defects at the interface), it has been proposed that inhomogeneous Li^+ transfer kinetics can lead to localized gradients in the lattice parameter of Li that, in turn, form stress concentrations potentially capable of causing the SSE to catastrophically fail by fracture [5, 6]. The foundation of this hypothesis is based on the argument that within these locally stressed volumes of metallic Li there exists a unique competition for stress relief that depends on the availability of microstructural defects within the stressed volume. Based on the self-limiting behavior of *bulk* metallic Li at or above room temperature (a homologous temperature, T_H, of ~0.69), the maximum sustainable pressure is nominally expected to be ~1 MPa or less. Recent studies have shown, however, that small volumes of pure metallic Li are capable of supporting more than 200 MPa [3, 4, 7]. This two-hundred-fold variation in stress is thought to be a direct reflection of the availability of microstructural defects needed to activate stress relief mechanism(s) within the stressed volume, e.g., shear driven glide or creep accommodated by intragranular dislocation mechanisms and/or stress-directed diffusion. The upshot is that these mechanical instabilities (stress concentrations) degrade device performance and potentially lead to catastrophic device failure by fracture of the SSE. In order to maximize device performance and safety, next-generation SSB materials will ideally be engineered to provide nominally stress-free, planar plating and stripping of a Li anode. To that end,

the goal of this work is to further elucidate the mechanism(s) of action that control the competition for stress relief in small, constrained volumes of crystalline metals subjected to high homologous temperatures.

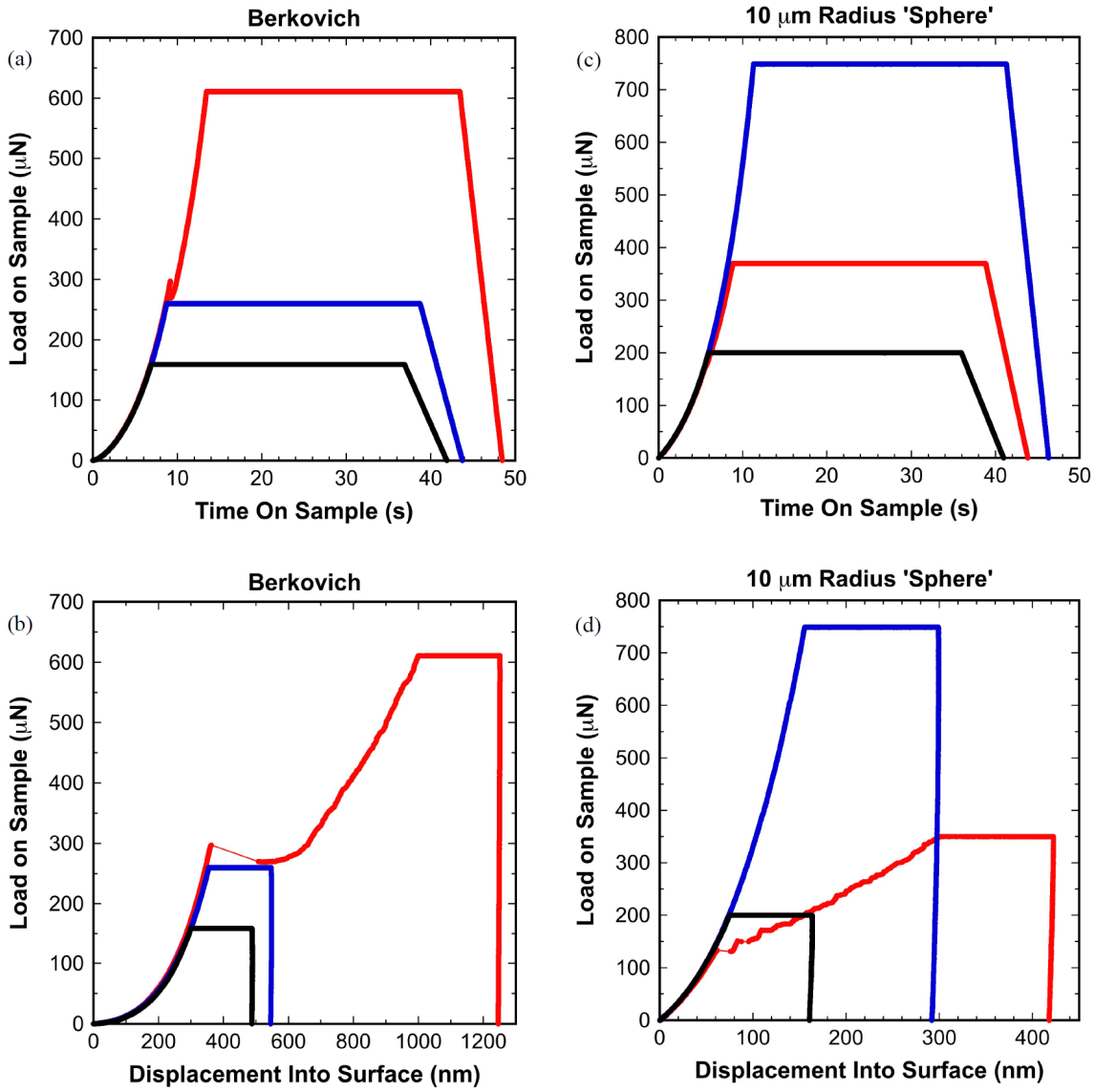

Figure 3.1. Representative load-time and load-displacement curves in high-purity, well-annealed indium. The data in (a) and (b) were acquired using a Berkovich indenter tip. The data in (c) and (d) were acquired using a 10 μm radius 'spherical' indenter tip. Sphere is in single quotes because at creep depths before the strain burst, the indenter tip geometry is not accurately described as a sphere, but rather a cone with half-included angle of approximately 84°.

3.3 Materials and Methods

High-purity, well-annealed indium is the focus of this investigation because at room temperature it exhibits a distinctive length scale dependent competition for stress relief that is very similar to that observed in high-purity lithium [2]. By contrast, the free surface of indium is stable in air and, therefore, unlike lithium, indium does not require testing in the controlled atmosphere of a glove box. A more complete description of the relevant similarities and properties of indium and lithium is available in reference 2. Following the same sample preparation procedures previously documented (casting and vacuum annealing at 110° C for 6 hours), the dislocation density of the indium test specimen is expected to be on the order of 10^4 or 10^5 cm^{-2}, which corresponds to a dislocation spacing in the range of ~100 to 30 μm, respectively. The average grain size was not directly measured, but the grains were clearly visible and ranged in size from ~2 to 3 mm in diameter.

3.3.1 Nanoindentation

Constant load and hold (CLH) creep experiments were performed in high-purity indium at room temperature using the iNano and the InForce50 nanomechanical actuator (Nanomechanics, Inc. KLA Tencor, Oak Ridge, Tennessee). The measurement system was isolated from mechanical vibrations using the 250BM-1 isolator (Minus K Technology, Inglewood, CA). Due to indium's strong propensity to creep at room temperature ($T_H \sim$ 0.69), no attempt was made to measure or correct for thermal drift. Instead, thermal stability was maximized by using an 8-hour start delay and running the experiments overnight. In addition, each test was completed in 50 s or less. The instrument's frame stiffness was taken to be 1.056×10^6 N/m. Twelve user defined test sites (4×3 arrays with 40 μm spacing in the x and y directions) were selected for each of the six target loads shown in Table 3.1. Using the optical targeting system of the iNano, test sites were selected within a single grain, albeit of unknown orientation. To examine the potential effects of

strain, the experiments were performed using two different indenter tip geometries: a diamond Berkovich and a sapphire sphere with a nominal radius of 10 μm. However, as shown in Appendix 3.A (Figure A3), over the indentation depths used to examine indium's creep behavior before the strain burst (≤ ~300 nm), the actual geometry of the sphere is more accurately described as a cone with a half-included angle of ~84°. Following the strain burst, the tip geometry transitions into that of a 10 μm radius sphere. To directly support rationalization of the indentation test results obtained using the Berkovich and the 'sphere', representative images of the residual hardness impressions were obtained using a high-resolution field emission scanning electron microscope (FE-SEM), the Hitachi S-4700 (Schaumburg, IL, USA).

Indium's room temperature creep behavior was captured during 30 s holds at each of the target loads identified in Table 3.1. In addition to the target loads, Table 3.1 summarizes the corresponding range in creep observed during each of the respective 30 s holds. The reported depths are averaged values and the percentages represent one standard deviation about the mean.

Table 3.1. Summary of the target loads and corresponding creep depths used to measure the room temperature stress exponent for creep, n, before and after the strain burst observed in high-purity, well-annealed indium.

	Berkovich	**10 μm radius sphere**
Before the strain burst		
Target load (μN)	162	200
$h_{creep\ start}$ (nm)	307 ± 0.4%	78 ± 2.9%
$h_{creep\ end}$ (nm)	486 ± 0.5%	164 ± 4.0%
h_{creep} (nm)	179	86
$h_{creep}/h_{creep\ start}$ (%)	58	110
Target load (μN)	260	750
$h_{creep\ start}$ (nm)	351 ± 1.8%	148 ± 4.3%
$h_{creep\ end}$ (nm)	547 ± 1.8%	280 ± 4.1%
h_{creep} (nm)	196	132
$h_{creep}/h_{creep\ start}$ (%)	56	89
After the strain burst		
Target load (μN)	615	360
$h_{creep\ start}$ (nm)	1040 ± 1.3%	306 ± 0.8%
$h_{creep\ end}$ (nm)	1260 ± 1.7%	425 ± 3.2%
h_{creep} (nm)	220	120
$h_{creep}/h_{creep\ start}$ (%)	21	39

For each of the CLH tests, the target loads were reached by controlling the loading rate, $\dot{P}$, through a feedback loop designed to achieve a prescribed $\dot{P}/P$ of 0.2 s^{-1}. This target was selected to minimize time and the potential effects of thermal drift. Figures 3.1(a) – (d) show representative load-time (P-t) and the corresponding load-displacement (P-h) curves for the test conditions described in Table 3.1.

3.3.2 Unique aspects of indium's indentation behavior before and after the strain burst

The stochastic strain bursts observed in indium (and lithium) are taken to be the direct outcome of a length scale dependent competition for stress relief. It has been proposed that the fundamental basis of this competition is directly linked to the probability of finding or not finding operable dislocations and/or operable dislocation multiplication sources within the stressed volume of material [2-4, 6]. Although this competition is in no way unique to indium and lithium, it has not been extensively examined in the literature because the high homologous temperatures required to observe this behavior have only become accessible to commercially available instrumented indentation in recent years. In this context, what makes indium and lithium unique is that the competition for stress relief is observable at room temperature, which corresponds to homologous temperatures of ~0.69 and ~0.66, respectively.

Before the strain burst, the creep experiments performed here correspond to indentation depths less than ~600 nm for the Berkovich and less than ~300 nm for the 10 μm radius sphere (see Table 3.1). At indentation depths less than 600 nm, previous experiments performed with the Berkovich (continuous normal loading) show the mean pressure supported by indium increases continuously with increasing depth. This unusual result (the complete opposite trend is typically observed in most metals) has been rationalized by proposing that before the strain burst, the dominant stress relief mechanism is diffusional flow along the interface between the indenter tip and indium surface (the diffusion length and, thus, the sustainable pressure increase with depth). A direct outcome of this hypothesis

is that unlike the plastic deformation typically observed in an indentation experiment, stress directed diffusion does not produce an elastically constrained plastic zone beneath the indenter tip. Instead, it is expected that the large dislocation spacing (~30 to 100 μm) and high homologous temperature enable the characteristic strain imposed by the indenter tip to create an elastic strain field (at some but not all test sites) that, through the elastic modulus and Hooke's law, generates stresses that drive interface diffusional flow. As previously documented, the corresponding stress is found to be considerably less than the theoretical elastic limit of $(G/(2\pi)$ to $G/30$, where G is the shear modulus, $G = 3.8$ GPa), and yet still well above the stress associated with an intrinsic indentation size effect (ISE) [8]. Moreover, as previously reported, the depth dependent mean pressure observed before the strain burst is completely opposite of the traditional ISE [2, 8].

After the strain burst, the creep experiments performed here correspond to indentation depths ranging from ~1000 to 1300 nm for the Berkovich and ~300 to 425 nm for the 10 μm radius sphere (see Table 3.1). These depths are well within the range of the ISE [8]. Previously documented experiments performed with the Berkovich at similar depths show that when subjected to continuous normal loading, the depth dependence observed in the mean pressure immediately following the strain burst is generally consistent with the ISE (hardness decreases with increasing depth) [2]. In addition, after the burst, the measured stress exhibits serrated flow, which is indicative of dislocations experiencing stick-slip behavior. Collectively, these observations suggest that over the range in creep depths examined here, the dominant stress relief mechanism after the burst is expected to be dislocation mediated glide and climb assisted glide. However, the ISE stipulates that additional geometrically necessary dislocations (GNDs) will be required to accommodate the gradient in strain imposed by the indenter tip [8]. The density of GNDs is expected to decrease with increasing depth, thus, the decreasing GND density will contribute to the decrease in stress with increasing depth. Since spherical indenter tips lack geometric self-similarity, the ISE is expected to manifest itself differently for the Berkovich and the sphere. As previously reported, it is also possible that after the strain burst, dynamic recovery and recrystallization enable GNDs and/or statistically stored dislocations to coalesce into cell walls or subgrains, thus providing an additional strengthening

mechanism. We also note that following the burst, the potential effects of work hardening and strain rate are poorly understood. The extent to which these factors may or may not contribute to strengthening is largely unknown.

3.3.3 Determining the stress exponent for creep, n

Determining constitutive creep parameters from nanoindentation experiments is an extensive and active field of research in and of itself. A comprehensive review of the experimental techniques and state-of-the-art analysis methods are available elsewhere [9-11]. In the context of determining n before and after the strain burst observed in indium, here we adopt the simplest form of the constitutive creep equation relating the stress, σ, and the steady state strain rate, $\dot{\epsilon}$,

$$\dot{\epsilon} = \alpha\sigma^n \tag{3.1}$$

where n is defined as the stress exponent for creep, the magnitude of which is taken to be characteristic of the dominant stress relief mechanism. As illustrated in Figures 3.1 (a) – (d), the P, h, and t data used to determine the $\dot{\epsilon}$, σ and n were acquired during 30 s holds at each of the six target loads (also see Table 3.1). Based on the data acquired during each hold, n is taken to be the slope of a linear fit to the plot, $\ln(\dot{\epsilon})$ versus $\ln(\sigma)$. For both the Berkovich and the spherical indenter tip, the strain rate during the 30 s hold is defined as

$$\dot{\epsilon} = \frac{\dot{h}}{h} \tag{3.2}$$

where $\dot{h}$ is the indenter tip velocity and h is the measured indentation depth. This definition was adopted for both tip geometries because h and $\dot{h}$ are directly measured during the

experiment. The stress, which is synonymous with the mean pressure or hardness, is defined as,

$$\sigma = \frac{P}{A} \tag{3.3}$$

where P is the applied load during the 30 s hold and A is the projected contact area. Experimentally, P is a controlled variable and A is calculated based on the measured or assumed mathematical relationship that describes how A physically changes with the indentation depth, h.

For the Berkovich indenter tip, the measured area function over contact depths ranging from 300 to 450 nm was found to be

$$A_{Berkovich} = 5.49h^{1.9} \tag{3.4}$$

where the coefficient has units of $m^{0.1}$ (see Appendix 3.A and Figure A2). It is further noted that here we take h to be equivalent to the contact depth, h_c. Beyond indium's large ratio of elastic modulus to yield strength, E/σ_y, justification for abandoning the Oliver-Pharr model and assuming $h = h_c$ is presented in a subsequent section. For the Berkovich, the lower limit of 300 nm corresponds to the minimum creep depth observed in indium and the upper limit of 450 nm corresponds to the maximum contact depth that could be achieved in the fused silica reference block at 90% of the actuator's 50 mN load limit.

Given the objective is to determine n and not α, an equally valid alternative method for determining A is to assume a perfect area function, i.e., $A = 24.56h^2$. In fact, other researchers have even set the coefficient equal to one [1]. Although this type of approach naturally forces an error in the estimate of σ, the error is systematic as long as the $A(h)$ relationship is constant. Subject to this constraint, the forced error in the calculation of A

and σ does not affect the estimate of n (the slope of $\ln(\dot{\epsilon})$ versus $\ln(\sigma)$). Despite the simplicity and utility of this approach, it is not the method employed here. As will be discussed in a subsequent section, our attempt at relating the magnitude of n to the mechanism of action controlling localized stress relief requires a more precise estimate of the functional dependence between A and h. In particular, the critical element is the magnitude of the exponent on h. As such, here we utilize the experimentally determined area function to define the $A(h)$ relationship over the relevant range in h, Eq. (3.4). A concise summary of the area function is available in Appendix I.

For a spherical indenter tip,

$$A_{sphere} = \pi a^2 \tag{3.5}$$

where a is the contact radius. Over contact depths ranging from 80 to 160 nm, the measured relationship between a and h was found to be

$$a = 0.17h^{0.74} \tag{3.6}$$

and, thus, the area function for the sphere is taken to be

$$A_{sphere} = 2.98 \times 10^{-2}\pi h^{1.48} \tag{3.7}$$

where the coefficient has units of $m^{0.52}$ (see Appendix 3A and Figure A3). For the sphere, the lower limit of ~80 nm corresponds to the minimum creep depth observed in indium and the upper limit of 160 nm is again a consequence of the actuator's load limit in conjunction with the silica reference block. A concise summary of the area function for the sphere (applicable only before the strain burst) is available in Appendix 3A.

3.3.4 Extrapolation of the indenter tip area functions, Eqs. (4) and (7)

Determining A over the full range of creep depths examined here requires the extrapolation of Eqs. (3.4) and (3.7) beyond the maximum calibration depths achieved in the fused silica reference block. For the Berkovich, extrapolation of the area function occurs over contact depths ranging from ~450 to 1300 nm. This is not an uncommon occurrence. Here we note the measured area function extrapolates smoothly and the area determined from Eq. (3.4) and the area measured from the residual hardness impressions at ~1300 nm are found to match within 2.4%. This indicates that extrapolation of the Berkovich area function (Eq. (3.4)) over contact depths ranging from ~450 to 1300 nm is valid and is not a significant source of error in determining A.

For the sphere, extrapolation of the area function occurs over contact depths ranging from ~160 to 450 nm. The unique challenge for many small radii spheres ($R \leq$ ~50 μm) is that at depths corresponding to a small fraction of R, the physical tip geometry is often not accurately described as a sphere [12]. In other words, when $h \ll R$, R is often found to be depth dependent. This is precisely the case here, as Eq. (3.7) represents a significant deviation from the ideal relation of $a = \sqrt{2Rh}$. In comparing the ideal tip geometry to the dimensions of the residual hardness impressions after the strain burst ($h \approx$ 450 nm), it is found they match to within 3.8%. This suggests that the measured area function transitions into the ideal tip geometry somewhere in the depth range of ~160 to 450 nm (1.6 to 4% of R). The unique problem here is that before the strain burst, the contact morphology exhibits significant pile up, which makes it very difficult to accurately assess the validity of the measured area function (see Figures 3.2 (a), (b), (d) and (e)). As shown in Appendix 3A, over the depth range of ~80 to 160 nm, the geometry of the sphere is more accurately described as a cone with a half-included angle of ~84°. Here we assume this geometry is followed until it transitions into the same area-to-depth relation as the ideal 10 μm radius sphere. Mathematically, this transition occurs at an indentation depth of ~250 nm, which

is within the expected range of 160 to 450 nm. This means that extrapolation of the measured area function for the sphere is theoretically limited to a maximum depth of ~250 nm, which is very close to the maximum creep depths observed before the strain burst (see Table 3.1). Following the strain burst, we implement the ideal area function for a sphere, $a = \sqrt{2Rh}$ (assuming $h \ll R$), which leads to

$$A_{sphere}\big|_{post\ strain\ burst} = 2\pi Rh \tag{8}$$

3.3.4.1 Justification for assuming $h = h_c$

Previously reported images of residual hardness impressions in high purity, well-annealed indium as well as the images obtained from this investigation (Figures. 3.2 (a) – (f)) show the contact morphology exhibits significant pile-up before the strain burst and virtually none after [2]. Collectively, these observations show the simplified definition of h_c adopted here is a reasonable approximation to make after the strain burst, but not before. Despite the obvious discrepancy that exists before the burst, the slope of $\ln(\dot{\epsilon})$ versus $\ln(\sigma)$, which is n, will be unaffected by the resulting underestimation of A and overestimation of σ as long as the pile-up geometry is self-similar over the range in displacement. In this way, the error in σ due to the pile-up observed before the burst is systematic and results only in a vertical shift of the data, not the slope. This rational also serves as the basis for the simplified area function implemented by others and mentioned previously, e.g., $A_{Berkovich} = 24.56{h_c}^2$ or even $A_{Berkovich} = {h_c}^2$ [1, 13].

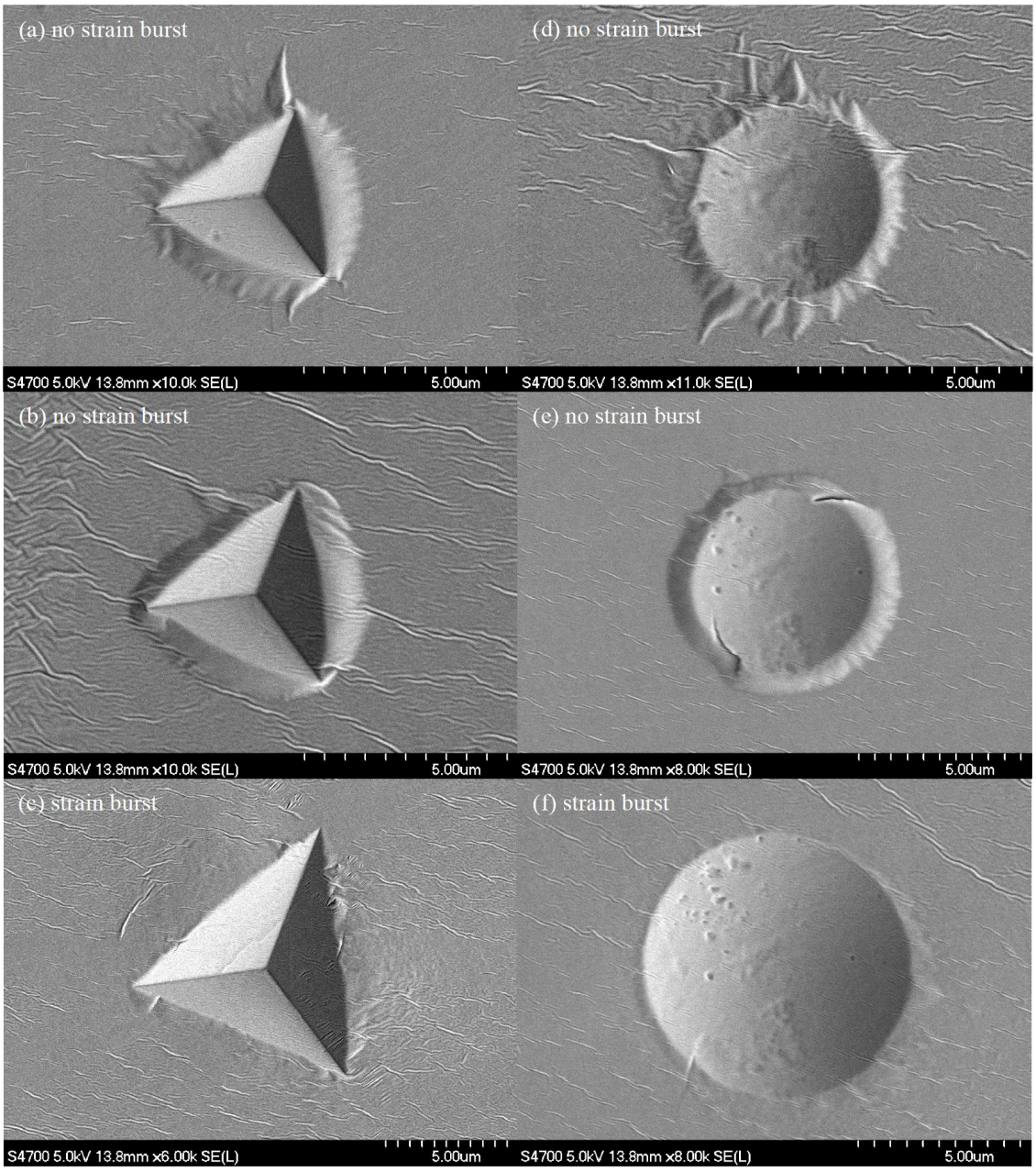

Figure 3.2. Representative residual hardness impressions in high-purity, well-annealed indium. Images(a) – (c) were generated by a Berkovich indenter tip at loads of 162, 260, and 615 μN, respectively. Images (d) – (e) were generated by a 10 μm radius 'spherical' indenter tip at loads of 200, 750, and 360 μN, respectively. The residual hardness impression from the sphere at 750 μN is smaller than the 360 μN impression due to the absence of the strain burst.

Well-validated models are capable of accounting for both pile-up and sink-in, however, the proposed mechanism of action, interface diffusion, is inconsistent with the dislocation mediated flow and elastically constrained plastic zone that form the basis of these models [10, 11]. Recalling that our goal is to determine the magnitude of n, the complexity of accurately accounting for pile-up is avoidable if, as stated above, the pile-up geometry is self-similar such that it creates a systematic error in the overestimation of σ. To a first order approximation, it will be shown that the simplified model adopted here results in predictions consistent with the experimental observations.

3.4 Results and Discussion

Analyzing the CLH indentation data in the manner described above, Figures 3.3 (a) – (d) show the average $\dot{\epsilon}$ versus σ and the corresponding $\ln(\dot{\epsilon})$ versus $\ln(\sigma)$. Although there is some discernable nuance in the linearity shown in Figs. 3.3 (a) and (c), the data are generally well described by the power law relation, $\dot{\epsilon} = \alpha\sigma^n$. Obtained from the curve fits shown in Figures 3.3 (a) – (d), the estimated values of n before and after the strain burst for both the Berkovich and the 10 μm radius sphere are summarized in Table 3.2. Before rationalizing these results, we present an important comparison to previously published data from similar experiments conducted over 20 years ago.

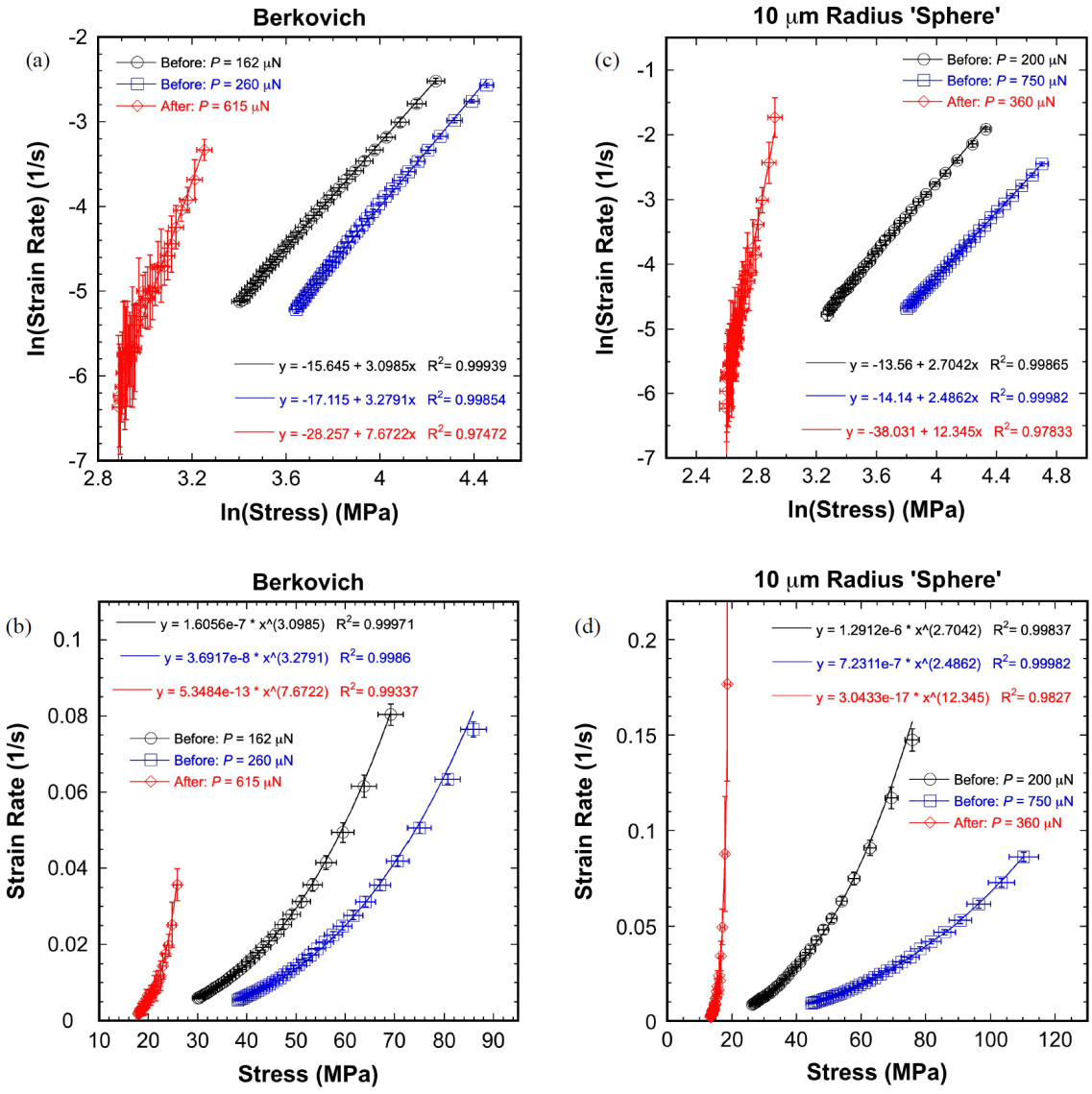

Figure 3.3. (a) and (b) show the measured strain rate-stress relationships acquired using the Berkovich indenter tip. (c) and (d) show the same relationships acquired using a 10 μm radius 'spherical' indenter tip. For both indenter tip geometries, Before and After refer to the characteristic strain burst observed in the load-displacement data.

Table 3.2. As measured by nanoindentation using the CLH method, the room temperature stress exponent for creep, n, evaluated before and after the strain burst observed in high-purity, well-annealed indium.

	Berkovich	10 μm radius sphere
Before the strain burst		
Load (μN)	162	200
Depth, $h_{creep\ start}$ (nm)	307	78
n (-)	3.1	2.7
Load (μN)	260	750
Depth, $h_{creep\ start}$ (nm)	351	148
n (-)	3.3	2.5
After the strain burst		
Load (μN)	615	360
Depth, $h_{creep\ start}$ (nm)	1040	306
n (-)	7.7	12.3
Increase in n after the burst	141%	373%

3.4.1 Previous measurements of n before and after the strain burst

Among the previous examinations of indium's indentation creep behavior, Feng and Ngan used a similar type of CLH experiment to evaluate n before and after the strain burst [1]. Their experiments were performed using a Berkovich indenter tip and n was determined from data acquired during what appears to be ~200 s hold. Both before and after the burst, Feng finds n to be depth dependent during the 200 s hold. Before the burst, Feng reports that n ranges from ~3 at the beginning of the hold to ~1.5 near the end. After the burst, n

is found to be ~6.2, but the value increases significantly near the end of the hold. Based on these values, Feng concludes the dominant stress relief mechanism operating before the strain burst is diffusional creep and dislocation creep after.

While Feng's values are somewhat similar to those reported here, rigorous comparisons are hindered by fundamental differences in the implementation of the experimental technique. Before the burst, Feng's experiments experience an uncontrolled load drop during the 200 s hold. The magnitude of the drop is determined by the product of creep distance and the spring constant of the indenter. The load drop is of particular importance in determining n before the strain burst because the product of the spring stiffness and the creep distance is a significant fraction of the applied load. Before the burst, the load drops continuously during the hold, from ~80 μN at the start to 60 μN at the end, a decrease of 25%. After the burst, the applied load increases to ~2.8 mN and, thus, the inherent load drop is significantly less, ~1%. The upshot is that before the burst, the depth dependent load in Feng's measurement potentially contributes to the observed depth dependence in n in a manner that is not understood.

After the burst, Feng's estimate of n comes from a target load of 2.8 mN and creep depths ranging from 2.2 to 3 μm. By comparison, these values are ~355% and ~117% larger than the target load and creep depths examined here, respectively. This is significant because the higher load and displacement utilized in Feng's analysis of n significantly decreases the potential influence of the ISE, which is thought to play an important role in the creep behavior examined here. As such, Feng's estimate of n after the burst is not directly comparable to the magnitude of n determined here.

In addition to Feng, the creep behavior of indium has also been examined by Lucas and Oliver [13]. Among the significant outcomes from their work, Lucas and Oliver find that at length scales commensurate with Feng's examination after the burst (generally beyond the ISE), $n = \sim 5$ and that it exhibits no depth dependence. By comparison, Feng finds $n = \sim 6.2$ and that the value changes with depth. The nature of the depth dependence discrepancy between Feng and Lucas is not well understood. We note, however, the

experiments performed by Feng were conducted using a commercially available nanoindenter while the experiments performed by Lucas were conducted using a custom built, and highly specialized high temperature mechanical properties microprobe specifically designed to overcome the challenges associated with micromechanical creep testing.

3.4.2 Qualitative comparisons among residual hardness impressions

Representative images of the residual hardness impressions obtained here are shown in Figures 3.2 (a) – (f). For both tip geometries, the surface morphology clearly transitions from significant pile-up before the strain burst, to virtually no pile-up after. This change in the morphology is taken to be representative of a major change in the deformation mechanism following the strain burst. Very similar results have been previously reported for the Berkovich [2]. In that study, analysis of the residual hardness impressions before the burst suggests the volume of indium displaced by the indenter tip is uniquely conserved by the pile-up, which is consistent with the hypothesized mechanism of interface diffusional flow [2].

At the lowest loads implemented here, Figures 3.2(a) and (d) show the surface morphology is considerably less uniform, particularly for the sphere. The undulating, starburst-like features emanating outward from the edges of the contact are poorly understood. Examination and rationalization of these features is beyond the scope of this work. Nevertheless, we speculate that the undulations in the surface may be the result of the Asaro-Tiller-Grinfeld (ATG) instability associated with elastic stress relaxation by surface diffusion [14, 15]. In this context, we conjecture that interplay between the stress and the surface free energy, which is affected by the local curvature, results in localized instabilities that manifest in nonuniform mass transport. Further examination and analysis of these unique features is left to future investigations.

3.4.3 After the strain burst: Relating n to the mechanism of action controlling localized stress relief

After the strain burst, the magnitude of n obtained from the experiments performed using the Berkovich increases from ~3.2 to 7.7 (an increase of 141%). In comparison, the value of n measured using the 10 μm radius sphere increases from ~2.6 to 12.3 (an increase of 373%). The strain burst itself is taken to signify the triggering of a dislocation multiplication source, resulting in an avalanche of dislocation motion. This is supported by the observed and previously documented transition from smooth, monotonically increasing load-displacement curves before the strain burst, to serrated, stochastic flow indicative of stick-slip behavior after the burst (also discernable in Figures 3.1 (b) and (d)) [2]. Considering the contact dimensions are more than two orders of magnitude smaller than the average grain size (1-2 mm), here we assume grain boundary stress relief mechanisms are largely inoperable. We also note the previously documented ISE observed after the burst is further evidence of dislocation mediated flow. Within this context, the measured values of n after the strain burst, 7.7 for Berkovich and 12.3 for the sphere, are taken to be representative of both dislocation glide and climb assisted glide.

The difference in n between the Berkovich (7.7) and the sphere (12.3) is not well understood. Recalling that the experiments performed with the sphere after the burst are well within range of the ISE ($h_{max} = \sim$425 nm $\leq 0.04R$, where R is the nominal tip radius of 10 μm) and that the ISE manifests itself differently for spheres and the Berkovich, it is not unreasonable to assume the ISE is at least a contributing factor to the difference in n observed after the burst. In addition to the ISE, differences in the imposed strain may also affect the amount and rate of work hardening. These important questions regarding the operational efficiency of stress relief mechanisms are left to future investigations.

3.4.4 Before the strain burst: Relating n to the mechanism of action controlling localized stress relief

Before the burst, both tip geometries yield values of n that are predominantly independent of the target load and the resulting displacement, suggesting that potential history effects are minimal. For both tip geometries, the measured n is significantly larger than 1, which, at macroscopic length scales, is the nominally expected value associated with stress directed diffusional flow [16]. Taken at face value, this result would seem to falsify the proposed hypothesis relating n to the mechanism of action enabling stress relief before the strain burst. However, in the following section, we present a new model that effectively rationalizes the measured values of n based on stress directed, interface diffusional flow. Within this context, the difference in n between the Berkovich ($\sim$3.2) and the sphere ($\sim$2.6) is taken to be a unique outcome of the different $A(h)$ relationships, not a change or transition in the mechanism of action enabling localized stress relief. As shown in Appendix 3A, converting the measured area functions to their respective equivalent cones, the Berkovich and sphere have half-included cone angles of 70.2 and 84°, respectively. Over the length scales examined here, the sharper angle of the Berkovich imposes a more severe shape change and, hence, creates a larger gradient in elastic strain. Through the elastic modulus and Hooke's law, this translates directly into higher stresses and steeper stress gradients driving the diffusive flow. In order to experience the same amount of stress relief, the Berkovich, by virtue of its geometry relative to the sphere, naturally requires a larger change in the strain rate, which under the conditions examined here, the indium appears capable of providing through a faster diffusion rate. This requirement is further corroborated by Figures 3.4 (a) and (b), which show that for the same decrease in stress, the Berkovich experiences a faster decrease in the velocity (higher rate of deceleration). Rationalized in this way, the difference in n between the Berkovich ($\sim$3.2) and the sphere ($\sim$2.6) is a unique consequence of the indenter tip geometry, not a change or transition in the stress relaxation mechanism. Additional evidence supporting this rationalization is provided in the form of the predicted relationship between the velocity and stress, which is presented in the following section.

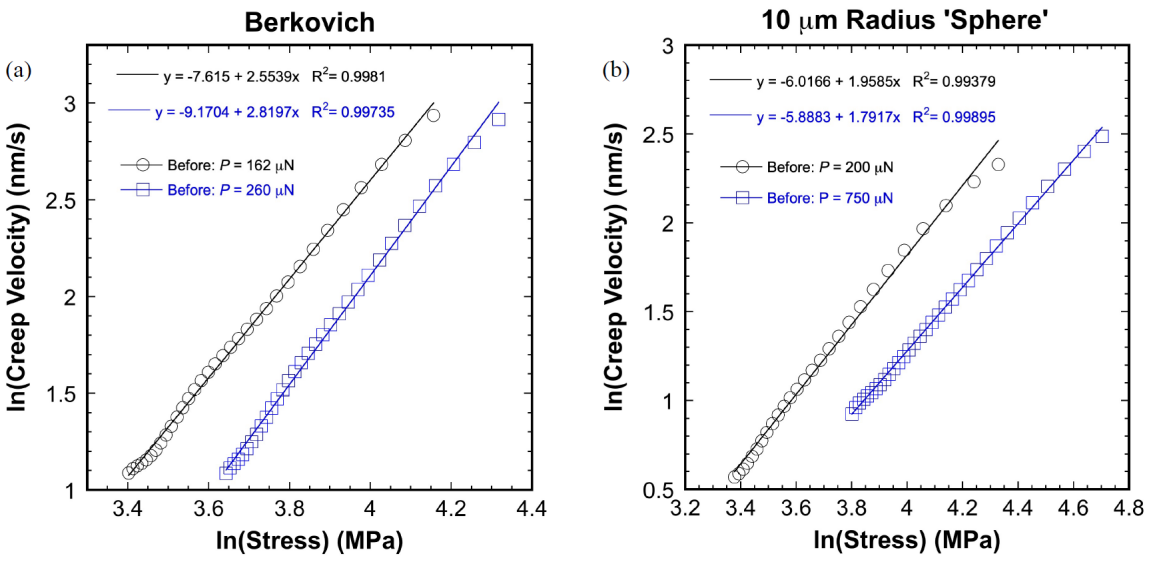

Figure 3.4. The velocity-stress relationships measured measured Before the strain burst using (a) the Berkovich indenter tip and (b) a 10 μm radius 'spherical' indenter tip.

3.4.5 A new model for localized, stress directed interface diffusional flow

Here, we consider the indentation creep of high-purity, well-annealed indium at a homologous temperature of ~0.69 in the context of an interface:surface diffusion mechanism. Mullins has shown that the local interface (or surface) velocity is determined by the divergence of the surface flux [17]. The velocity of a rigid shape then requires a constant flux divergence over the surface of the shape if it is to remain constant [17, 18]. For the indentation problem, the flux divergence is considered constant over the indenter:indium interface at each point in time, with the required spatial distribution of the chemical potential required for constant flux divergence adjusting as the indenter tip velocity changes. Using the Mullins small slope approximation for the indenter:interface shape, the solution for the chemical potential, μ (J/atom), is obtained from the solution of the differential equation for the constant flux divergence (over the interface) in polar coordinates,

$$-\frac{\dot{h}}{B} = constant = \frac{1}{r}\frac{\partial}{\partial r}\left(\frac{1}{r}\frac{\partial u}{\partial r}\right) \tag{3.9}$$

which assuming symmetry about $r = 0$ yields

$$\mu = C - \frac{\dot{h}}{B}r^2 \tag{3.10}$$

where $\dot{h}$ is the indentation velocity, B is a diffusion coefficient term, $B = D_s\delta/(k_BT)$ (atom m^3/(Js)), D_s is the self-diffusion coefficient (m^2/s), δ is the surface layer thickness (m), k_B is the Boltzmann constant (J/(K·atom)), T (K) is the absolute temperature, r is the radial position (m), and C is an integration constant (J/atom) [18]. The coefficient C may be determined by noting that the average chemical potential under the indenter tip must correspond to the mean pressure, σ, supporting the indenter through the integral

$$\int_0^a \left(C - \frac{\dot{h}}{B}r^2\right) r\, dr\, \frac{1}{\pi a^2} = \Omega\sigma \tag{3.11}$$

which determines

$$\Omega\sigma = -\frac{\dot{h}a^2 - 2BC}{4\pi B} \tag{3.12}$$

allowing for the solution for the integration constant

$$C = \frac{\dot{h}a^2 + 4\pi B\Omega\sigma}{2B} \tag{3.13}$$

and, thus, the chemical potential distribution along the indenter:indium interface,

$$\mu_{interface} = \frac{\dot{h}a^2 + 4\pi B\Omega\sigma}{2B} - \frac{\dot{h}}{B}r^2 \tag{3.14}$$

where Ω is the atomic volume (m^3/atom).

At the intersection of the indenter:indium interface with the indium free surface, referred to as the triple junction, we note the gradient in the chemical potential must be continuous and, the gradient sets the equation for the velocity, $\dot{h}$, of the indenter tip. Although the exact form of the free surface chemical potential, $\mu_{free\ surface}$, is unknown, here we assume it is equal to the elastic strain energy/atom, $U_{free\ surface}$, as described in references [14] and [15]. In doing so, the gradient in the chemical potential evaluated at the triple junction ($d\mu_{interface}/dr$ at $r = a$) is equal to the gradient in free surface elastic strain energy/atom evaluated at the triple junction ($dU_{interface}/dr$ at $r = a$). Here, we approximate the elastic strain energy distribution along the indenter:indium interface through the elastic solution for a pressurized hollow sphere of radius, h [19]. The stress parallel to the free surface, designated σ_{rr}, is estimated to have the form

$$\sigma_{rr} = -\sigma\left(\frac{h}{r}\right)^3 \tag{3.15}$$

Taking the elastic strain energy to be $\sigma^2/(2E)$, then, the elastic strain energy/atom along the indenter:indium interface can be estimated as

$$U_{interface} = \Omega\frac{{\sigma_{rr}}^2}{2E} = \Omega\frac{\sigma^2}{2E}\left(\frac{h}{r}\right)^6 \tag{3.16}$$

and the corresponding gradient in the elastic strain energy/atom evaluated at the triple junction ($r = a$) is then,

$$\left.\frac{dU_{interface}}{dr}\right|_{r=a} = \Omega \left.\frac{d({\sigma_{rr}}^2/2E)}{dr}\right|_{r=a} = -\Omega\frac{3\sigma^2 h^6}{Ea^7} \tag{3.17}$$

The imposed boundary condition at the triple junction sets $\left.\frac{d\mu_{interface}}{dr}\right|_{r=a}$ equal to $\left.\frac{d\mu_{free\,surface}}{dr}\right|_{r=a}$. Thus, the boundary condition can be re-stated as

$$\left.\frac{d\mu_{interface}}{dr}\right|_{r=a} = \left.\frac{dU_{interface}}{dr}\right|_{r=a} \tag{3.18}$$

which, through the differentiation of Eq. (3.14), Eq. (3.18) gives

$$\frac{2\dot{h}a}{B} = \Omega\frac{3\sigma^2 h^6}{Ea^7} \tag{3.19}$$

The diffusion-based analysis presented in this section culminates in Eq. (3.19), which now serves as the basis for determining the relationship between $\dot{h}$ and σ, and, ultimately, $\dot{\epsilon}$ (or $\dot{h}/h$) and σ. As previously noted, this analysis only applies to the creep behavior observed before the strain burst.

3.4.6 Comparison to the model for nanoindentation creep from Li and Warren

The surface diffusion limited strain rate analysis of Li and Warren for a cone shaped indenter uses a similar approach to the analysis presented here except for the application

of the free surface elastic strain energy boundary condition (Eq. 3.18) and the manner in which the velocity of the indenter tip is mathematically represented (Eq. 3.10 here versus Eq. A2.8 from Li and Warren) [20]. Eq. 3.10 defines the indentation velocity as given by the divergence in diffusion potential while Eq. A2.8 indirectly defines the indentation velocity in terms of the gradient in the diffusion potential, which is inconsistent with Mullins [20]. Here, Eq. 3.18 considers that the diffusion along the free surface adjacent to the indenter:surface interaction contributes to the kinetics of stress relaxation via surface diffusion. Certainly, the residual hardness impressions previously documented and those reported here show surface morphology changes consistent with mass transport at the free surface during the creep process [2].

3.4.7 Berkovich Indenter Tip Geometry

Based on the measured area function for the Berkovich (see Appendix 3A), the relationship between a and h for this tip's equivalent cone is

$$a = 1.29h^{0.948} \tag{20}$$

Solving Eq. (3.19) for $\dot{h}$ and substituting the $a(h)$ relationship for the equivalent cone (Eq. (3.20)) gives,

$$\dot{h} = \frac{C_1 B \Omega \sigma^2}{E h^{1.58}} \tag{21}$$

To eliminate the depth dependence, we utilize the relationship between a and σ,

$$\sigma = \frac{P}{\pi a^2} \tag{3.22}$$

or

$$a = 1.29h^{0.948} = \frac{\sqrt{P}}{\sqrt{\pi}\sqrt{\sigma}} \tag{3.23}$$

Solving Eq. (3.23) for h and substituting into Eq. (3.21) gives the relationship between $\dot{h}$ and σ as

$$\dot{h}_{Berkovich} = \frac{C_2 B\Omega\sigma^{2.83}}{EP^{0.83}} \tag{3.24}$$

which predicts that a log-log plot of $\dot{h}$ versus σ will have a slope of 2.83, which is consistent with the experimental observations shown in Figure 3.4 (a). The relationship between $\dot{\epsilon}$ and σ is derived by dividing both sides of Eq. (3.24) by h, yielding

$$\left.\frac{\dot{h}}{h}\right|_{Berkovich} = C_3 \frac{B\Omega\sigma^{3.36}}{EP^{1.36}} \tag{3.25}$$

which predicts that a log-log plot of $\dot{h}/h$ (or $\dot{\epsilon}$) versus σ will have a slope of 3.36, which is consistent with the experimental observations shown in Figures 3.3 (a) and (b).

3.4.8 Spherical Indenter Tip Geometry

Solving Eq. (3.19) for $\dot{h}$ and substituting the $a(h)$ relationship for the sphere, $a = C_4\, h^{0.75}$, gives

$$\dot{h}_{sphere} = \frac{C_4 B \Omega \sigma^2}{E} \tag{3.26}$$

which indicates that a log-log plot of $\dot{h}$ versus σ has a slope of 2, which is consistent with the experimental observations shown in Figure 3.4 (b). The relationship between $\dot{\epsilon}$ and σ is derived by dividing both sides of Eq. (3.26) by h, yielding

$$\left.\frac{\dot{h}}{h}\right|_{sphere} = \frac{C_4 B \Omega \sigma^2}{E}\frac{1}{h} \tag{3.27}$$

To eliminate the depth dependence, we utilize the relationship between a and σ,

$$\sigma = \frac{P}{\pi a^2} = \frac{P}{\pi (C_6\, h^{0.75})^2} \tag{3.28}$$

Solving Eq. (3.28) for h gives

$$h = C_7 \frac{P^{0.67}}{\sigma^{0.67}} \tag{3.29}$$

Substituting Eq. (3.29) into Eq. (3.27) and simplifying yields,

$$\left.\frac{\dot{h}}{h}\right|_{sphere} = C_8 \frac{B\Omega\sigma^{2.67}}{EP^{0.67}} \tag{3.30}$$

which predicts that that a log-log plot of $\dot{h}/h$ (or $\dot{\epsilon}$) versus σ will have a slope of 2.67, which is also consistent with the experimental observations shown in Figures 3.3 (c) and (d).

Equations (3.25) and (3.30) are also of interest because they predict a load dependent shift in the stress:strain rate behavior. That is, for a given stress, the measured strain rate ratio at two different loads is expected to follow the ratio of the two constant loads to the power of -1.36 for the Berkovich and -0.67 for the sphere. For example, consider the Berkovich data. At a stress of 47 MPa, the strain rate ratio at the two different loads is 2.1, with Eq. (3.25) predicting a ratio of 1.9. Similarly, for the sphere, at a stress of 50 MPa, the strain rate ratio at the two different loads is 4.4, with Eq. (3.30) predicting a ratio of 2.4. The general dependence on load is correctly predicted by the model, but the magnitude of the load effect is underestimated for the 'sphere.' We speculate that this discrepancy is due to inaccuracies imposed by the forced extrapolation of the area function for the 'sphere.'

3.5 Conclusions

Using instrumented indentation performed with a diamond Berkovich and a sapphire sphere with a nominal radius of 10 μm, the stress exponent for creep of high-purity, well-annealed indium has been measured before and after a characteristic strain burst signaling an abrupt transition in the mechanism of action that controls stress relief.

1. Before the strain burst, experiments performed at two different loads using the Berkovich indenter tip yield stress exponents of $n = 3.1$ and $n = 3.3$, indicating the creep behavior is nominally history independent.
2. Before the strain burst, experiments performed at two different loads using the 10 μm spherical indenter tip yield stress exponents of $n = 2.7$ and $n = 2.5$, again, indicating the creep behavior is nominally history independent.
3. Before the strain burst, the measured stress exponents were rationalization using a new model based on stress directed diffusional flow along the interface between the indenter tip and the surface of the test specimen. Based on the new model, the predicted stress exponents for the Berkovich and sphere are not 1 (the expected value for diffusional flow at bulk or macroscopic length scales), but rather 3.36 and 2.67, respectively. These predictions are consistent with the experimental observations. Comparing the expected and measured values of n, the relative error for the Berkovich and sphere are 4.8 and 2.6%, respectively.
4. Before the strain burst, the difference in n between the Berkovich and sphere is not due to a change in the stress relaxation mechanism, but rather a direct outcome of the indenter tip's physical geometry, or more specifically, the relationship between the projected contact area and the indentation depth.
5. After the strain burst, experiments performed using the Berkovich and sphere yield stress exponents of $n = 7.7$ and $n = 12.3$, respectively. These values are taken to be representative of dislocation glide and climb assisted glide. The difference in n between the Berkovich and the sphere is not well understood, but thought to be a direct outcome of the indentation size effect and potential contributions from differences in the imposed strain, which is expected to affect the amount and rate of work hardening.

A Appendix 3.A. Indenter Tip Characterization

A.1 The diamond Berkovich indenter tip

The representative P-h curves in Figure 3.1 (b) show that experiments performed with the Berkovich correspond to creep depths ranging from ~300 to 1300 nm. As shown in Figure A.1, analysis of elastic P-h data from experiments performed on single crystal sapphire, the tip defect at the apex of the Berkovich is thought to be ~160 nm. Considering the two-dimensional analog of an ideal Berkovich to be a cone with a half-included angle of 70.3°, the transition from the tip defect to the Berkovich geometry is nominally expected to occur at a depth of ~10 nm, which is well below the minimum creep depth of ~300 nm. This suggests that at $h \geq$ ~300 nm, the relationship between the contact depth, h_c, and the projected contact area, A, known as the indenter tip's area function, should be accurately described by the tip manufacturer's measured lead term alone.

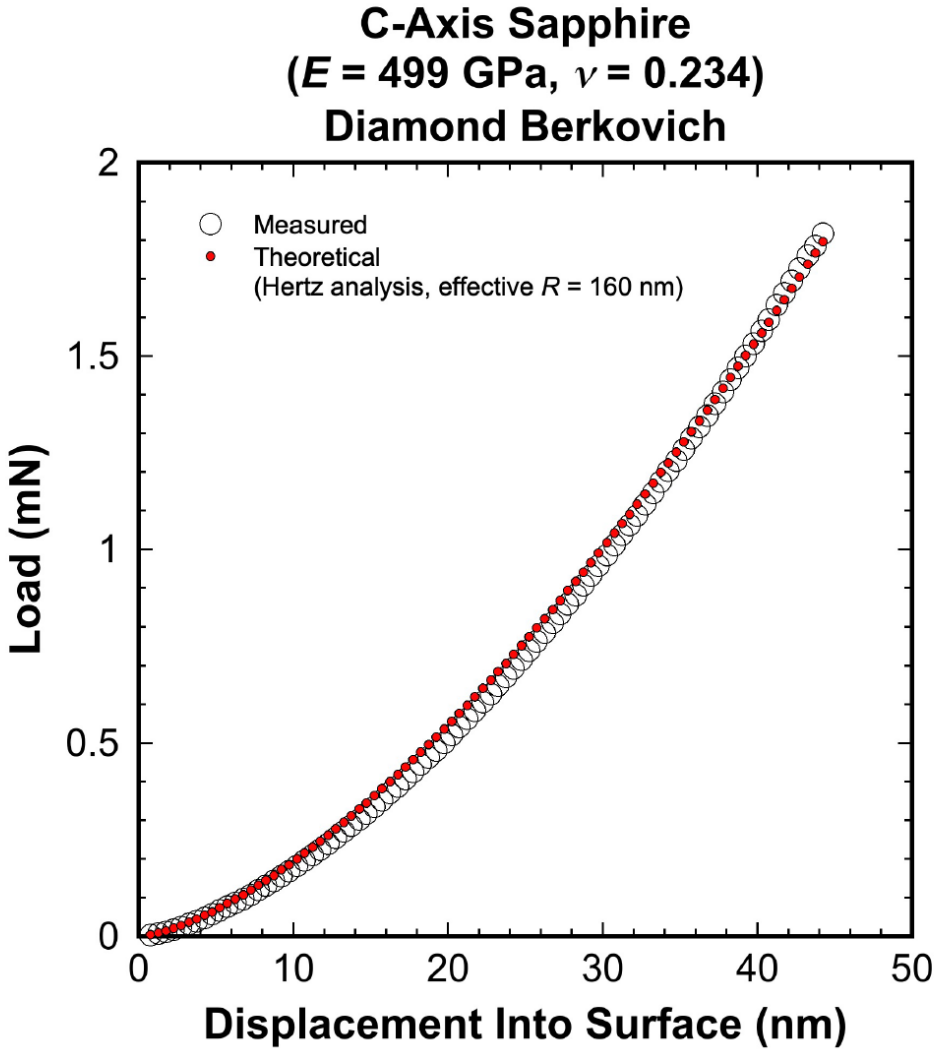

Figure A.1. Direct comparison between the theoretical and experimentally measured elastic load-displacement data acquired using the Berkovich indenter tip and C-axis sapphire. As per the theoretical relationship of Hertz, the effective radius of the tip defect is approximately 160 nm.

The area function for the Berkovich was experimentally determined using a frequency specific nanoindentation technique coupled with a fused silica reference block [21, 22]. The elastic properties of the reference block (Young's modulus and Poisson's ratio) were previously measured using ultrasonic techniques. Details of procedure used to determine

the area function are well-documented elsewhere [21-23]. Here we present only the highlights relevant to the creep experiments performed in indium.

Implementing a frequency specific nanoindentation technique, the elastic contact stiffness, S, was measured continuously as a function of depth to ~635 nm (90% of the actuator's maximum load). Through the universal stiffness relation,

$$E_r = \frac{\sqrt{\pi}}{2}\frac{1}{\beta}\frac{S}{\sqrt{A}} \tag{A1}$$

the corresponding A was calculated as a continuous function of depth. The geometric constant β was taken to be 1.0 and E_r, the reduced elastic modulus is given by

$$E_r = \left(\frac{1-\nu_i{}^2}{E_i} + \frac{1-\nu^2}{E}\right)^{-1} \tag{A2}$$

where ν_i and E_i are Poisson's ratio and the elastic modulus of the diamond indenter, 0.07 and 1141 GPa, respectively, and ν and E are the ultrasonically measured values of the silica reference block, 0.19 and 73 GPa, respectively. The corresponding contact depth, h_c, was calculated using the Oliver-Pharr model,

$$h_c = h - \epsilon\, P/S \tag{A3}$$

where h is the displacement into the surface of the test specimen, P is the applied load and ϵ for the Berkovich indenter is taken to be 0.75. Figure A.2 shows the calculated A as a function of h_c and the corresponding curve fit, which gives the indenter tip's area function over contact depths ranging from ~300 to 450 nm. The lower limit of 300 nm corresponds

to the minimum creep depth achieved in indium and the upper limit of 450 nm is fixed by the load limit of the actuator. The projected contact area directly measured from the residual hardness impressions following the strain burst (no discernable pile-up) is found to match the extrapolated best fit area function to within 3.4%. As a point of reference, we note the coefficient obtained by forcing the exponent on h_c to 2 matches the manufacturer's measured lead term to within 0.5%.

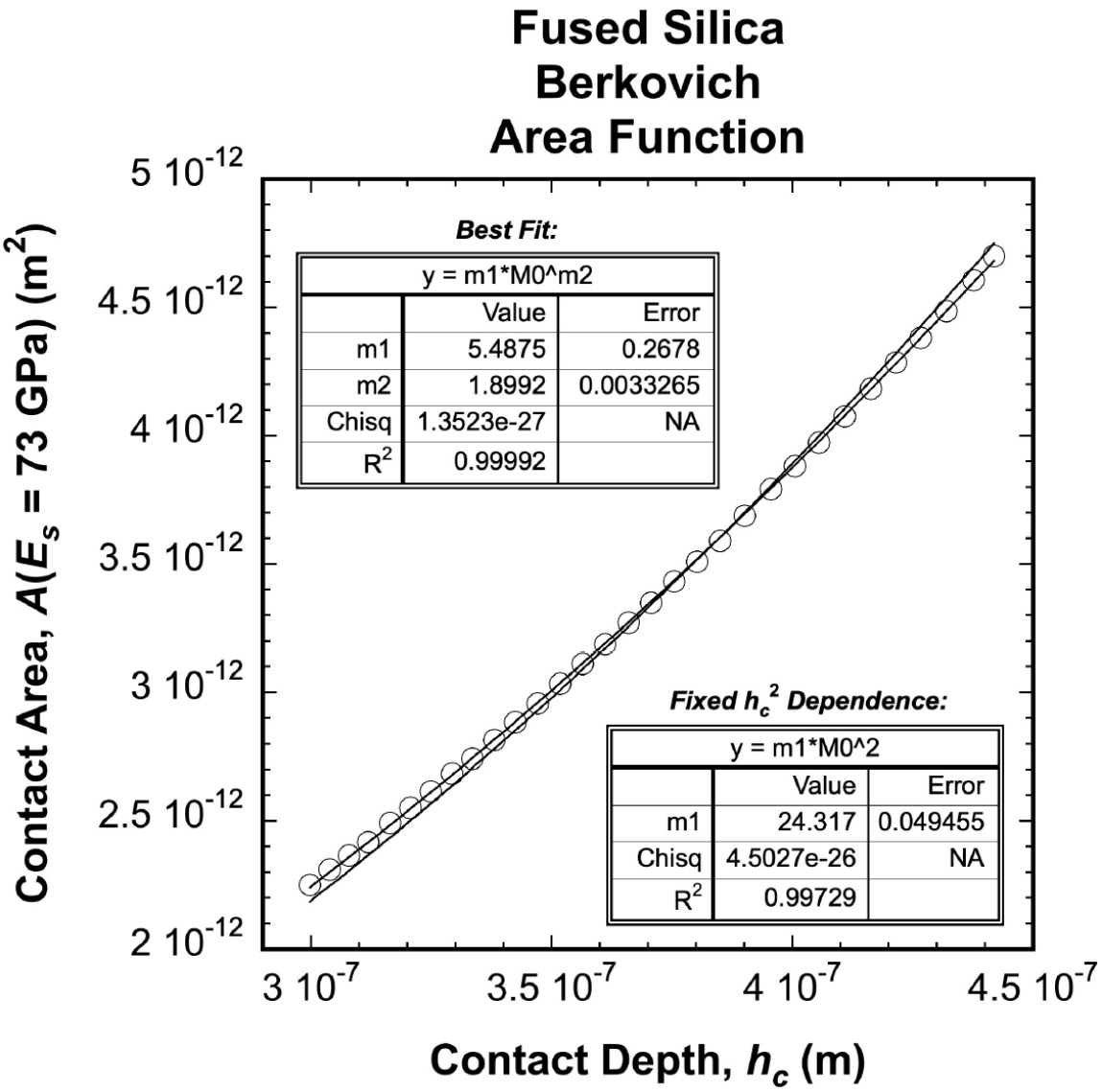

Figure A.2. The experimentally determined area function for the Berkovich indenter tip over contact depths (creep depths) ranging from 300 to 450 nm.

A.2 The 10 μm radius sapphire spherical indenter tip

As previously described, the area function for the sphere is piecewise,

$$A_{sphere} = \begin{cases} 2.98 \times 10^{-2} \pi {h_c}^{1.48} & \text{for } 80 \leq h_c \leq \sim 250 \text{ nm (before the strain burst)} \\ 2\pi R h_c & \text{for } h_c \geq \sim 250 \text{ nm (after the strain burst)} \end{cases} \quad \text{(A4)}$$

recalling that we assume $h_c = h$.

After the strain burst, the area function is taken to be that of a perfect sphere with a radius of 10 μm. Before the strain burst, the area function was experimentally determined using the same frequency specific technique implemented for the Berkovich. The contact is taken to be elastic and over the depth range of interest, the indenter tip geometry is closely approximated by a parabola of revolution ($2Rh_c \gg {h_c}^2$). As such, Eq. (A1) reduces to

$$S = 2aE_r \quad \text{(A5)}$$

where a is the contact radius. Figure A.3 shows the calculated a as a function of h_c and the corresponding curve fit, which gives the indenter tip's area function over contact depths ranging from ~380 to 160 nm. The Hertz solution for an elastic contact gives $h_c = h/2$. Alternatively, the Oliver-Pharr model (Eq. (A3)) can be used, as it reduces to the Hertz solution in the limit of an elastic contact.

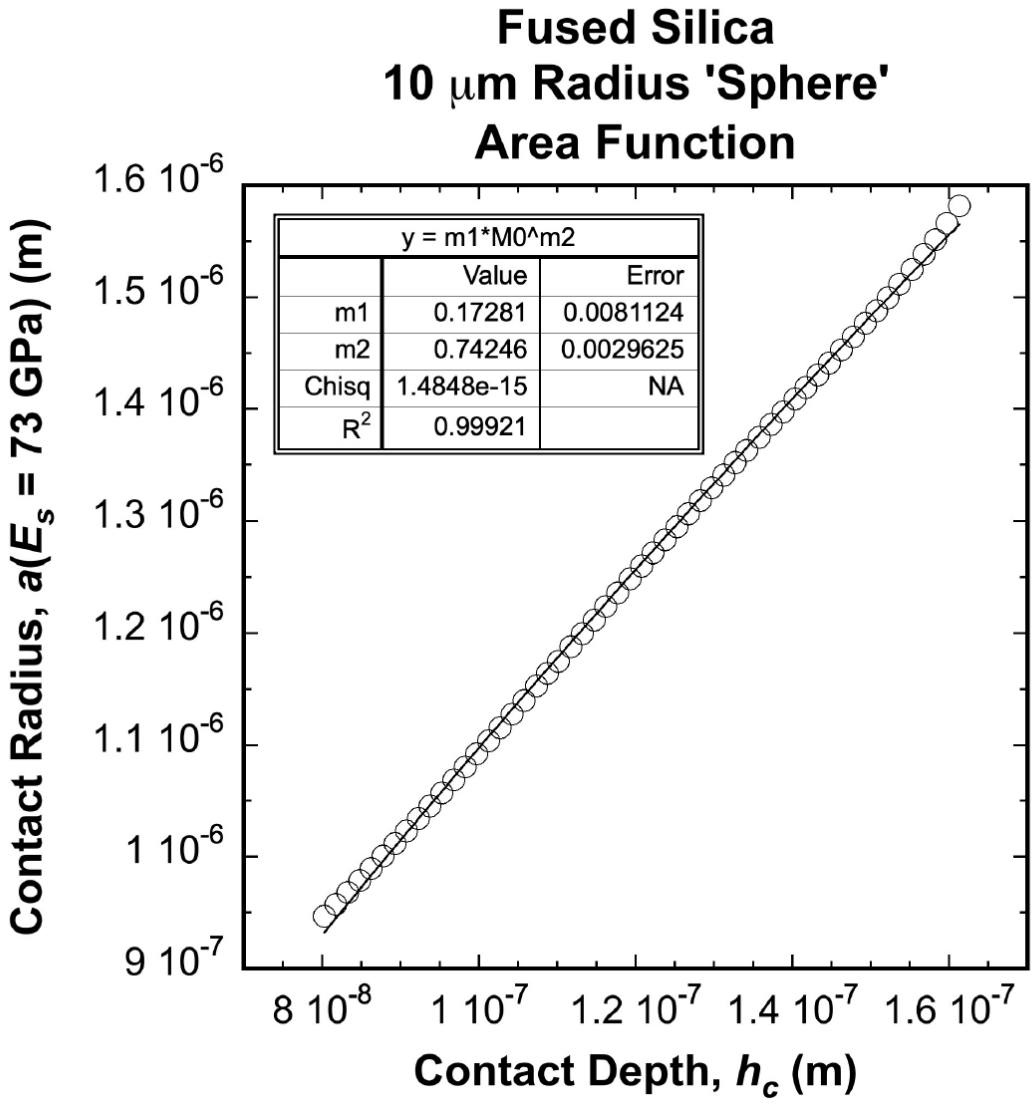

Figure A. 3. The experimentally determined area function for the 10 μm radius 'spherical' indenter tip over contact depths (creep depths) ranging from 80 to 160 nm.

3.6 References

1. G. Feng, A. Ngan, Creep and strain burst in indium and aluminium during nanoindentation, Scripta materialia 45(8) (2001) 971-976.

2. F. Mallakpour, M. Kasraie, E.G. Herbert, P.S. Phani, S.A. Hackney, Length-scale-dependent stress relief mechanisms in indium at high homologous temperatures, J. Mater. Res. 36 (2021) 2444-2455.

3. E.G. Herbert, S.A. Hackney, N.J. Dudney, V. Thole, P.S. Phani, Nanoindentation of high purity vapor deposited lithium films: A mechanistic rationalization of diffusion-mediated flow, J. Mater. Res. 33(10) (2018) 1347-1360.

4. E.G. Herbert, S.A. Hackney, N.J. Dudney, V. Thole, P.S. Phani, Nanoindentation of high purity vapor deposited lithium films: A mechanistic rationalization of the transition from diffusion to dislocation-mediated flow, J. Mater. Res. 33(10) (2018) 1361-1368.

5. P. Albertus, V. Anandan, C. Ban, N. Balsara, I. Belharouak, J. Buettner-Garrett, Z. Chen, C. Daniel, M. Doeff, N.J. Dudney, B. Dunn, S.J. Harris, S. Herle, E.G. Herbert, S. Kalnaus, J.A. Libera, D. Lu, S. Martin, B.D. McCloskey, M.T. McDowell, Y.S. Meng, J. Nanda, J. Sakamoto, E.C. Self, S. Tepavcevic, E. Wachsman, C. Wang, A.S. Westover, J. Xiao, T. Yersak, Challenges for and Pathways toward Li-Metal-Based All-Solid-State Batteries, ACS Energy Letters 6(4) (2021) 1399-1404.

6. E.G. Herbert, N.J. Dudney, M. Rochow, V. Thole, S.A. Hackney, On the mechanisms of stress relaxation and intensification at the lithium/solid-state electrolyte interface, J. Mater. Res. 34(21) (2019) 3593-3616.

7. C. Xu, Z. Ahmad, A. Aryanfar, V. Viswanathan, J.R. Greer, Enhanced strength and temperature dependence of mechanical properties of Li at small scales and its implications for Li metal anodes, Proc. Natl. Acad. Sci. U.S.A 114(1) (2017) 57-61.

8. G.M. Pharr, E.G. Herbert, Y.F. Gao, The indentation size effect: A critical examination of experimental observations and mechanistic interpretations, Ann. Rev. Mat. Res. 40 (2010) 271-292.

9. C. Su, E.G. Herbert, S. Sohn, J.A. LaManna, W.C. Oliver, G.M. Pharr, Measurement of power-law creep parameters by instrumented indentation methods, Journal of the Mechanics and Physics of Solids 61(2) (2013) 517-536.

10. A. Bower, N.A. Fleck, A. Needleman, N. Ogbonna, Indentation of a power law creeping solid, Proc. R. Soc. Lond. A 441(1911) (1993) 97-124.

11. R.S. Ginder, W.D. Nix, G.M. Pharr, A simple model for indentation creep, J. Mech. Phys. Solids 112 (2018) 552-562.

12. E.G. Herbert, W.C. Oliver, G.M. Pharr, On the measurement of yield strength by spherical indentation, Philosophical Magazine 86(33-35) (2006) 5521-5539.

13. B. Lucas, W. Oliver, Indentation power-law creep of high-purity indium, Metallurgical and Materials Transactions A 30(3) (1999) 601-610.

14. R.J. Asaro, W.A. Tiller, Interface morphology development during stress corrosion cracking: Part I. Via surface diffusion, Metallurgical and Materials Transactions B 3 (1972) 1789–1796.

15. M.A. Grinfeld, Instability of the interface between a nonhydrostatically stressed elastic body and a melt, Akademiia Nauk SSSR Doklady 290(6) (1986) 1358-1363.

16. T.G. Langdon, Identifying creep mechanisms in plastic flow, Zeitschrift für Metallkunde 96(6) (2005) 522-531.

17. W.W. Mullins, Theory of Thermal Grooving, J. Appl. Phs. 28 (1957).

18. S.H. Yu, S.A. Hackney, On the shape change of a nonequilibrium faceted microcrystal, Scripta Metallurgica et Materialia 24(11) (1990) 2077-2082.

19. A.F. Bower, Applied Mechanics of Solids. http://solidmechanics.org/Text/Chapter4_1/Chapter4_1.php#Sect4_1_4.

20. W. Li, R. Warren, A model for nano-indentation creep, Acta metallurgica et materialia 41(10) (1993) 3065-3069.

21. W.C. Oliver, G.M. Pharr, An Improved Technique for Determining Hardness and Elastic Modulus Using Load and Displacement Sensing Indentation Experiments, Journal of Materials Research 7(6) (1992) 1564-1583.

22. W.C. Oliver, G.M. Pharr, Nanoindentation in Materials Research: Past, Present, and Future, MRS Bulletin 35 (2010).

23. W.C. Oliver, G.M. Pharr, Measurement of hardness and elastic modulus by instrumented indentation: Advances in understanding and refinements to methodology, Journal of Materials Research 19(1) (2004) 3-20.

4 Chapter 4: The Next Steps: Knowledge Gaps, Hypotheses, and Experiments

Through instrumented indentation, optical and scanning electron microscopy, and etch pit analysis, chapters 2 and 3 provide significant experimental evidence of the unique competition for stress relief in small, constrained volumes of indium at room temperature. Coupled with the proposed rationalizations, these data and experimental observations provide unique insight into the mechanisms of action controlling stress relief before and after the strain burst observed in indium. Building on this framework, a more complete and comprehensive understanding of small-scale plasticity at high homologous temperatures can be developed by filling additional knowledge gaps. Key among them are the following: (1) What is the post-test microstructure of indium before and after the strain burst? (2) Do measurements of the pile-up volume observed before the strain burst correlate directly to the volume of indium displaced by the indenter tip? (3) How does the length scale dependent competition for stress relief change with temperature, strain, and strain rate? (4) Following the strain burst, does the avalanche of dislocation motion contribute to strengthening or is the strengthening negated by simultaneous recovery and recrystallization?

(1) What is the post-test microstructure of indium before and after the strain burst?

Beyond the etch pit analysis performed in the as-annealed condition (before testing), characterization of the post-test microstructure of indium was not performed in this study because of the unique challenges associated with creating suitable test specimens. Due to indium's high homologous temperature at room temperature, the unique challenge is developing a technique for creating sufficiently thin cross-sections through residual hardness impressions without enabling relaxation in the form of diffusional flow or dislocation motion. The concern is that localized heating and removal of the constraint from focused ion beam milling will further activate these stress relaxation mechanisms. As such, meaningful comparisons of the microstructure before and after the strain burst could

be significantly confounded by differences in the constrained microstructure versus the locally heated and unconstrained microstructure observed in the transmission electron microscope. Among the techniques that could potentially address this issue, in-situ transmission electron microscopy (TEM) experiments cannot solve this problem, as the lack of constraint would render meaningful comparisons impossible. Cryogenic TEM of the residual harness impressions is a viable path forward, but the challenge of cryogenic cross-sectioning and transfer to the TEM still remain. Based on the conclusions presented in chapters 2 and 3, filling this knowledge gap relies not on hypothesis testing, but rather on providing direct experimental evidence of the before and after microstructure that either supports or refutes the following: Plastic deformation observed before the strain burst results in no significant change in the dislocation density relative to the as-annealed condition. Following the strain burst, it's a bit trickier. While the expectation is that following the burst, the dislocation density naturally increases, the timescale over which dynamic recovery and recrystallization influence the structure is largely unknown.

(2) Do measurements of the pile-up volume observed before the strain burst correlate directly to the volume of indium displaced by the indenter tip?

Chapter 2 presents a unique experimental method and model for evaluating the volume of indium piled up around the faces of the residual hardness impression. This analysis is central to the hypothesis that the dominant stress relief mechanism before the strain burst is diffusional flow along the interface between the indenter tip and the surface of the test specimen. A direct outcome of this hypothesis is that the volume of indium displaced by the indenter tip is uniquely conserved in the form of pile-up surrounding the periphery of the contact. As shown in chapter 3, the morphology of the pile-up becomes significantly less uniform as the length scale decreases. While the nature of the star-burst like patterns is not well understood, conservation of volume is still taken to be a key assumption in relation to the stress relaxation mechanism. Additional experimental evidence of the pile-up volume should be obtained as a function of length scale. It is proposed that reasonable estimates of the pile-up volume could be acquired using atomic force microscopy.

(3) How does the length scale dependent competition for stress relief change with temperature, strain, and strain rate?

Based on the conclusions presented in chapters 2 and 3, the stress directed diffusion that occurs before the strain burst is expected to be significantly affected by temperature, strain, and strain rate. The basic hypothesis is as follows: If subjected to higher homologous temperatures, then indium will support less stress at the same strain and strain rate because of the reduced activation energy for stress directed diffusion and the higher diffusion coefficient. To test this hypothesis, nanoindentation experiments would be performed at elevated temperatures using multiple indenter tip geometries and a range of strain rates limited by the thermal stability of the lab at the low end and the system's measurement time constants at the high end. In addressing the active stress relief mechanism before the strain burst (stress directed diffusion), additional hypotheses could readily be constructed based on the expectation that faster strain rates will lead to higher stresses because of shorter diffusion times. Similarly, higher strains are expected to lead to higher stresses because of longer diffusion lengths. Of particular interest, these experiments will also provide new insight into the transition from diffusion to dislocation mediated flow. At elevated temperatures, dislocation multiplication sources presumably require the same physical room to operate, but they clearly have a lower activation energy. How the coupling between these two variables effects the transition from diffusion to dislocation mediated flow is an important element that has yet to be investigated in indium.

(4) Following the strain burst, does the avalanche of dislocation motion contribute to strengthening or is the strengthening negated by simultaneous recovery and recrystallization?

After the strain burst, any dislocation multiplication that results in strengthening is expected to inhibit stress relaxation. In the context of solid-state-batteries, this outcome promotes a less stable interface between a lithium anode and a solid electrolyte separator, as the strained volume is capable of supporting larger stress concentrations. To examine

this issue, the following hypothesis is proposed: If a plastically deformed volume of indium is subjected to nanoindentation at a high homologous temperature, then in comparison to its undeformed condition, the indium will support more stress at the same strain, indentation depth, and strain rate because the increase in dislocation-dislocation interactions results in strengthening.

This hypothesis assumes that dynamic recovery and recrystallization do not completely eliminate the new dislocations created by the strain burst and subsequent deformation. As such, it is expected that instrumented indentation experiments performed within the strained volume will not exhibit the transition from diffusion to dislocation mediated flow. In addition, the measured stress will be significantly lower relative to unstrained indium and the stress-depth relationship will exhibit a traditional intrinsic indentation size effect. To test this hypothesis, the following two-step procedure is proposed. As schematically illustrated in Figure 4.1, the heavily deformed volume of indium is created first by performing an impact experiment. This step is carried out by positioning the indenter over the targeted test site, lifting the indenter to the top of its range of travel, and then hurtling the indenter towards the surface with the maximum load available. Using the InForce 50 actuator, the resulting impact creates a residual hardness impression in indium that is nominally 350 μm along each of the 3 faces.

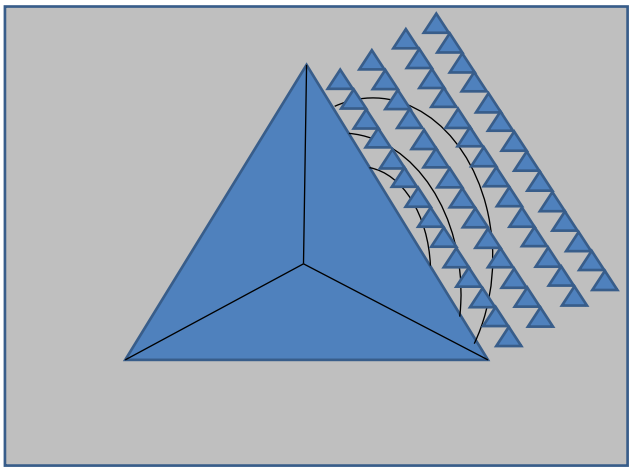

Figure 4.1. Schematic illustration of the indent pattern used to test the hypothesis stated above.

As schematically illustrated in Figure 4.1, the plastic zone is expected to extend radially outward from the center of the impact impression, creating a gradient in plastic strain. As the figure shows, the next step is to perform 3 prescribed arrays of indents along each face of the impact crater. These experiments will be conducted at a constant strain rate and terminated at a depth of 1 μm, resulting in residual hardness impressions that are nominally 7.5 μm along each face. From each test site, the hardness will be measured as a continuous function of depth. These results will enable the assessment of potential changes in the dislocation density by virtue of the change in hardness relative to the unstrained indium. In addition, the absence of strain bursts in the load-displacement data will further corroborate elimination of the competition for stress relief.